Revealing intact neuronal circuitry in centimeter-sized formalin-fixed paraffin-embedded brain

Ya-Hui Lin, Li-Wen Wang, Yen-Hui Chen, Yi-Chieh Chan, Shang-Hsiu Hu, Sheng-Yan Wu, Chi-Shiun Chiang, Guan-Jie Huang, Shang-Da Yang, Shi-Wei Chu, Kuo-Chuan Wang, Chin-Hsien Lin, Pei-Hsin Huang, Hwai-Jong Cheng, Bi-Chang Chen & Li-An Chu**

Y. H. Lin, L. W. Wang, Y. C. Chan, Prof. S. H. Hu, S. Y. Wu, Prof. C. S. Chiang, Prof. L. A. Chu
Department of Biomedical Engineering and Environmental Sciences
National Tsing Hua University
Hsinchu, 300044, Taiwan
E-mail: lachu@mx.nthu.edu.tw

Y. H. Lin, L. W. Wang, Prof. L. A. Chu
Brain Research Center
National Tsing Hua University
Hsinchu, 300044, Taiwan

Prof. Y. H. Chen
Institute of Biomedical Sciences
Academia Sinica
Taipei, 115024, Taiwan

G. J. Huang, Prof. S. W. Chu
Department of Physics
National Taiwan University
Taipei, 106216, Taiwan

Prof. S. D. Yang
Institute of Photonics Technologies
National Tsing Hua University
Hsinchu, 300044, Taiwan

Dr. Kuo-Chuan Wang
Department of Neurosurgery
National Taiwan University Hospital
Taipei, 100225, Taiwan

Dr. Chin-Hsien Lin
Department of Neurosurgery
National Taiwan University Hospital
Taipei, 100225, Taiwan

Dr. Pei-Hsin Huang
Department of Pathology
National Taiwan University Hospital
Taipei, 100225, Taiwan

Prof. Hwai-Jong Cheng

Institute of Molecular Biology
Academia Sinica
Taipei, 115024, Taiwan

Prof. Bi-Chang Chen
Research Center for Applied Sciences
Academia Sinica
Taipei, 115024, Taiwan
E-mail: chenb10@gate.sinica.edu.tw

Keywords: tissue clearing, multiplexed staining, formalin-fixed paraffin-embedded, archived tissues, whole-mouse brain imaging

Abstract

Tissue clearing and labeling techniques have revolutionized brain-wide imaging and analysis, yet their application to clinical formalin-fixed paraffin-embedded (FFPE) blocks remains challenging. We introduce MOCAT, a novel method for efficiently clearing and labeling centimeter-thick FFPE specimens using elevated temperature and concentrated detergents. MOCAT with multi-round immunolabeling reveals neuron circuitry regulating multiple neurotransmitter systems in a whole FFPE mouse brain, and is able to be used as the evaluation of disease treatment efficiency. MOCAT also supports expansion microscopy and can be performed on a non-sectioned 15-year-old FFPE specimen. Thus, MOCAT represents a feasible approach for researching archived FFPE specimens for future neuroscientific and 3D neuropathological analyses.

1. Introduction

Clinical brain tissues play a critical role in unraveling the molecular mechanisms underlying neurological diseases and facilitating the development of effective treatments,[1–3] and also represent an invaluable resource for retrospective studies on rare diseases or conditions with long-term outcomes.[4] Currently, the majority of archived clinical specimens are stored in the form of formalin-fixed paraffin-embedded (FFPE) blocks. Advanced molecular analysis tools—such as chromatin immunoprecipitation (ChIP), DNA/RNA sequencing (DNA/RNA-seq), and Luminex assays—have been performed on FFPE specimens to enable comprehensive analysis from genomic, transcriptional, and proteomic perspectives.[3,5–7] However, image-based qualification and quantification of FFPE samples remains limited to performing chemical staining and immunohistochemistry on thin sections. Although whole-slide imaging enables unbiased analyses of entire tissue sections,[3,8–10] its two-dimensional (2D) nature cannot provide the 3D information required for accurate quantification. Such quantification in neurobiological contexts is crucial for evaluating neuronal damage and neuroprotection, including neuronal cell counts and the extent of necrosis. Moreover, such 2D-based techniques also fail to reveal structural changes within target tissues.

Tissue clearing protocols,[11–14] in combination with deep-tissue immunolabeling [15–17] and optical sectioning microscopy techniques,[18–20] represent powerful tools for collecting 3D information at a subcellular resolution from centimeter-scale specimens. Tissue clearing techniques render biological tissues transparent by removing components that induce refraction index mismatching, which is mainly attributable to two factors, i.e., light absorption due to pigments or biological chromophores and light scattering mainly caused by lipids.[11,21] In current tissue clearing protocols, samples are fixed with 4% paraformaldehyde (PFA) for approximately 24 hours before undergoing delipidation steps that involve solvents,[22–24] aqueous solutions with denaturing reagents or detergents,[25–28] or protection with chemicals that create crosslinks to withstand harsh electrophoretic delipidation.[29–31] Such protocols now enable imaging of whole-rodent bodies.[32,33] and even entire

26 human organs at the cellular or subcellular level,[34] facilitating detailed and comprehensive analyses
27 of intact biological systems. However, FFPE specimens have not reaped the benefits of these advanced
28 techniques. For instance, although tissue clearing approaches such as CUBIC, iDISCO, CLARITY,
29 and passive SDS treatment have been applied previously to FFPE specimens,[35–40] they have only
30 yielded immunolabeling depths of 1-2 mm, underscoring the need for a procedure tailored to FFPE
31 samples in order to achieve centimeter-scale tissue clearing and labeling.

32 Our objective was to develop a protocol capable of rendering centimeter-scale FFPE specimens
33 optically transparent and suitable for deep immunolabeling. To this end, we took account of two critical
34 issues. First, successful immunohistochemistry of FFPE tissue sections requires antigen retrieval to
35 restore target conformation and expose masked epitopes.[41,42] Secondly, despite xylene treatment
36 during paraffin processing and dewaxing protocols removing a substantial proportion of FFPE tissue
37 lipids, certain phospholipids persist within the lipid bilayer, impeding antibody penetration and
38 maintaining opacity.[38,43] Therefore, we aimed to devise a procedure that achieves efficient antigen
39 retrieval and delipidation for centimeter-scale FFPE specimens. Here, we present Multiplex labeling
40 Of Centimeter-sized Archived Tissue (MOCAT), a pipeline that employs an optimized heat-induced
41 antigen retrieval technique to achieve that goal. We validated the effectiveness of MOCAT using FFPE
42 human brain tissues and entire mouse brains. Using MOCAT, we demonstrate the possibility of
43 conducting multiple rounds of immunolabeling, which allowed characterization of the same brain
44 tissue using six different neuronal markers and revealing neuronal circuitry. We further demonstrate
45 volumetric quantification by means of MOCAT on intact FFPE mouse brains, with statistical analysis
46 of the FFPE samples resulting in identical trends to the results determined for fresh brains. We also
47 showcase the broad applications of MOCAT by successfully conducting volumetric imaging of mouse
48 brain archived in FFPE blocks for a period of 15 years, as well as the compatibility of this apporach
49 with expansion microscopy.

50

2. Results

2.1. Optimized antigen retrieval: Delipidation and epitope recovery of FFPE specimens

SDS is a detergent commonly used for lipid removal in tissue clearing methods. It is also known as an antigen retrieval agent and has been used to enhance immunolabeling signals in cells,[44] cryosections,[45] formalin-fixed human brains,[46] and epithelia of the pancreas, liver and lung.[47] Therefore, we began optimizing tissue clearing by applying two types of SDS-based approaches, passive and active, to FFPE mouse brain hemispheres and then evaluated their impacts on antigen retrieval/delipidation by means of electrophoretic immunolabeling.[15] For the passive approach, we applied a FLASH protocol published previously involving sample incubation in an SDS-based solution (4% SDS and 200 mM borate) at 54 °C for antigen retrieval and tissue clearing of epithelial cells and abdominal organs.[47] For the active approach, we employed SDS-based electrophoresis at 42 °C for 48 hours. We observed that both FLASH-processed and SDS-electrophoresed samples showed weak tyrosine hydroxylase (TH, a marker of dopaminergic neurons) signal (Figure S1a). Additionally, we noticed that the FLASH-processed samples had almost no signal of NeuN (a marker of neuronal nuclei, Figure S1b left), and exhibited strong non-specific background noise (Figure S1a left). The presence of this background noise is considered an indicator of inadequate antigen retrieval.[48]

We found that FLASH-processed samples displayed weak tyrosine hydroxylase (TH, a marker of dopaminergic neurons) signal and almost completely lacked signal of NeuN (a marker of neuronal nuclei) (Figure S1a left, 1b left). We also observed that the SDS-electrophoresed sample only possessed weak TH-positive signal, as well as strong non-specific labeling (Figure S1a right), with this latter considered an indicator of inadequate antigen retrieval.[48]

These results imply insufficient antigen retrieval using the SDS approaches, likely due to the low-temperature experimental conditions. In 1991, Shi et al. published a heat-induced epitope retrieval (HIER) method utilizing a temperature of 100 °C,[49] which now represents the most broad-spectrum

75 antigen retrieval protocol for FFPE tissue sections. Superheating (i.e., temperatures >100 °C) in
76 pressure cookers has been reported to enhance immunohistochemistry signal intensity and
77 stability.[50,51] However, heating with a classical antigen-retrieval citrate buffer (10 mM sodium citrate,
78 pH 6.0) at 121 °C for 10 minutes in a pressure cooker, a condition appropriate for routine FFPE sections,
79 only resulted in weak immunostaining signals of NeuN and SMI312 (a pan-neurofilament marker) in
80 the middle of a 2-mm-thick FFPE mouse brain block (Figure S1b middle). Since dewaxed and
81 rehydrated FFPE specimens still have residual phospholipids that prevent antibody penetration,[38,43]
82 we added 1% SDS into the citrate buffer to increase the delipidation capability of the HIER approach
83 and found that NeuN and SMI312 signals were significantly enhanced (Figure S1b right). However,
84 deploying SDS at such high temperatures also resulted in tissue expansion and fragility (Figure S1b,
85 gross view), prompting us to search for a detergent condition that could achieve sufficient delipidation
86 while retaining tissue integrity.

87 Accordingly, we tested four additional detergent conditions: 1% Tween 20; 1% Triton X-100; 1%
88 sodium cholate (NaC); and 1% CHAPS. Tween 20 and Triton X-100 are commonly used to disrupt
89 cell membranes in immunohistochemistry. NaC and CHAPS have higher critical micelle
90 concentrations and form smaller micelles than SDS, and both have been reported as being more
91 efficient than SDS with respect to active electrophoretic delipidation[52] and passive delipidation,[34]
92 respectively. All tests were performed on 2-mm-thick FFPE mouse brain blocks with citrate buffer (10
93 mM sodium citrate, pH 6.0) at 121 °C for 10 minutes in a pressure cooker. First, we assessed amounts
94 of residual lipids by staining with DiD (a lipophilic dye with an excitation wavelength at 649 nm).
95 Undelipidated and SDS-delipidated (hereafter referred to as PFA-SDS) mouse brain blocks, as well as
96 dewaxed FFPE mouse brain blocks without HIER, were also stained as controls. To prove that DiD
97 signal quantification could be used to reflect amounts of residual lipids in tissue sections, we compared
98 DiD signal across the FFPE group without HIER, the undelipidated group and the PFA-SDS group
99 (**Figure 1A**, left panel). The FFPE group without HIER exhibited a higher DiD signal intensity than

100 the PFA-SDS group but lower than that of the undelipidated group, supporting partial lipid removal
101 during the paraffin processing and dewaxing process. Among all of the test groups subjected to varied
102 heated detergent conditions, only the 1% Tween 20 condition presented significantly lower lipid
103 content compared to the FFPE without HIER group (p-value = 0.0035), achieving the same level of
104 delipidation as the PFA-SDS group (p-value = 0.999) (Figure 1A, right panel). We also performed Oil
105 red O staining to visualize the residual lipids and tissue morphology under bright-field microscopy
106 (Figure S2).

107 Next, we evaluated the efficiency of antigen retrieval by conducting immunolabeling with NeuN
108 and SMI312 antibodies on all of the test groups and examined the signals at the center of each FFPE
109 specimen. We found that the 1% Tween 20 group displayed the sharpest and clearest neuronal nuclei
110 and axon bundles with a high signal-to-background ratio, indicating both successful delipidation and
111 antigen retrieval (Figure 1B, panel 2). Interestingly, for the 1% Triton X-100, 1% NaC and 1% CHAPS
112 groups, the fluorescence intensity of neuronal nuclei were even lower than the background signal,
113 implying that heating these detergents might hinder nuclear epitopes (Figure 1B, panels 3, 4 and 5).
114 We also examined the gross appearance of each group upon heating, which confirmed that the 1%
115 Tween 20 group retained good sample integrity without apparent changes in size or color (Figure 1C).
116 Therefore, we employed 1% Tween 20 in citrate buffer with heating in a pressure cooker at 121 °C for
117 10 minutes as the critical step of our MOCAT pipeline for delipidation and antigen retrieval of
118 centimeter-scale FFPE specimens.

119 **2.2. The MOCAT pipeline**

120 We illustrate the complete MOCAT pipeline in Figure 1D. To retrieve a specimen from a FFPE
121 block, the paraffin is first melted at 65-70 °C, before dewaxing at room temperature using xylene and
122 sequentially rehydrating the tissue with alcohol. It is important to note that when working on a large
123 sample, the dewaxing time should be increased to avoid opacity caused by residual wax due to
124 insufficient dewaxing. Opacity can be eliminated through repeated dehydration and dewaxing steps

125 (Figure S3b), with extended dewaxing times or repeated dewaxing steps not affecting tissue structure
126 or antigenicity (Figure S3 and S4). A typical dewaxing timeframe for paraffin sections of less than 20
127 μm thickness is ~20 minutes, with complete dewaxing of an entire mouse brain or similarly-sized
128 sample achievable within 24 hours (see Materials and Methods). Optimal dewaxing times for tissue
129 sizes between these two extremes warrant further testing.

130 The rehydrated FFPE samples are then treated with epoxy[31] and immersed in the optimized
131 antigen retrieval solution (10 mM sodium citrate, 1% Tween 20, pH 6.0) at 37 °C for 24 hours, before
132 then being heated to 121 °C for 10 minutes. The samples are then subjected to active immunolabeling
133 (see Materials and Methods). After staining, the specimen is immersed in 4% PFA for 24 hours to fix
134 the antibodies bound to epitopes, matched for the refractive index (RI), and imaged by means of
135 lightsheet microscopy. Figure S5 shows the gross views of the same mouse brain after undergoing 4%
136 PFA fixation, paraffin processing, optimized antigen retrieval, and RI-matching, demonstrating
137 intactness of the brain shape and preservation of tissue integrity. To enable 3D phenotyping and
138 proteomic investigations, a multi-round staining protocol involving photobleaching and classic heat-
139 induced antigen retrieval can also be included. In this study, unless otherwise specified, all MOCAT-
140 processed whole mouse brains had been stored in paraffin blocks for two to six months before the
141 experiments and underwent active labeling after heating with 1% Tween 20.

142 To further verify MOCAT's efficacy in removing lipids from whole mouse brains, we employed
143 coherent anti-Stokes Raman scattering (CARS), a spectroscopic technique for detecting vibrational
144 responses of specific molecular structures (Figure 1E). In contrast to a dewaxed FFPE mouse brain
145 (Figure 1D, left) for which we observed CARS signals from axon bundles, thus indicating the presence
146 of myelinated lipids, both the FFPE-MOCAT-processed and PFA-SDS-treated mouse brain samples
147 displayed significantly lower CARS signals (Figure 1E, middle and right, respectively; quantification
148 in Figure 1F), confirming removal of myelinated lipids.

149 **2.3. The MOCAT pipeline enables immunolabeling and registration of intact FFPE mouse brain**

150 Previous studies have confirmed that transcriptomic and proteomic data are equally preserved in
151 FFPE sections and fresh-frozen sections. To assess biomarker preservation within a spatial context, we
152 investigated patterns of anti-TH antibody labeling in FFPE-MOCAT-processed mouse brains (**Figure**
153 **2**A). We observed consistent distributions of dopaminergic neurons in key tissue regions, including
154 the striatum, nigrostriatal fiber tracts, substantia nigra, ventral tegmental area, pontine reticular nucleus,
155 and lateral reticular nucleus, aligning with the findings of a prior study[16] (Figure 2A, left) and
156 matching results from Allen Brain Atlas registration[53] (Figure 2A, right). Furthermore, we compared
157 the volume of each brain region between the left and right hemispheres, which revealed minimal
158 sample distortion (Figure 2B). Our investigation extended to a 2-mm-thick mouse brain that had been
159 preserved in an FFPE block for 15 years. By applying MOCAT, we unveiled clear clusters of
160 dopaminergic neurons at a cellular resolution in that specimen (Figure 2C). These results confirm the
161 feasibility of deploying MOCAT for long-term stored FFPE blocks, even without the need for
162 sectioning, enabling effective retrieval of information on spatial biomarkers comparable to that
163 obtained from freshly fixed samples. We also applied MOCAT to 3-month fixed mouse brain
164 hemispheres (Figure S6). Although the long-term fixed specimens exhibited reduced TH intensity and
165 S/N ratio, the major dopaminergic regions were labeled, and magnified images revealed clear details
166 of cell bodies and neuronal fibers. These results suggest that MOCAT has the potential to be applied
167 to long-term fixed specimens.

168 **2.4. A tailored MOCAT+ pipeline enables multi-round immunolabeling of human brain tissues**
169 **and whole mouse brains**

170 Next, we investigated if MOCAT-processed whole-brain FFPE samples could be subjected to a
171 multi-round staining process, a strategy commonly used for multiplexed immunolabeling. Chemical
172 elution techniques utilizing detergents, reducing reagents, and denaturing reagents have been
173 developed previously and tested on thin paraffin sections or cryosections. For thick sections, the
174 CLARITY protocol published in 2013 involves incubation in 4% SDS solution, which was first

175 demonstrated on a 1-mm-thick mouse hippocampus specimen. However, based on our preliminary
176 experiments, we found that post-staining fixation is required to maintain signals in a centimeter-sized
177 sample (i.e., a whole mouse brain) (Figure S7) and the post-fixed antibodies cannot be completely
178 stripped using SDS-based stripping protocols (Figure S8). We also observed that fixation after staining
179 hindered subsequent rounds of staining, although this impediment could be overcome by traditional
180 heat-induced epitope retrieval (referred to hereafter as classical HIER to avoid confusion with the
181 aforementioned optimized antigen retrieval protocol) (Figure S9). To overcome the difficulty of
182 antibody stripping due to post-fixation, which is required for centimeter-sized specimens, we
183 developed MOCAT+ to include a multi-round immunolabeling protocol utilizing photobleaching and
184 classical HIER (Figure 1D). After imaging, we photobleached transparent RI-matched samples using
185 a 100W LED white light to quench the previously labeled fluorophores (Figure S10). The selected
186 duration of bleaching is dependent on sample thickness; overnight bleaching is sufficient for tissue
187 samples of <500 μm thickness, whereas ~72 hours are required for thicker samples such as whole
188 mouse brains (a thickness of 0.8-1 cm). Bleached specimens are then subjected to classical HIER to
189 restore the antigenicity hindered by post-staining PFA fixation. The brain shape and structural integrity
190 remained after 4 rounds of immunolabeling, and there is no cross-reactivity in subsequent rounds of
191 immunostaining following bleaching (Figure S11).

192 To explore the potential of revealing multiple neuronal circuitry in the whole FFPE mouse brain
193 using MOCAT+, we performed a six-round immunolabeling procedure for TH, tryptophan
194 hydroxylase 2 (TPH2), calbindin, parvalbumin (PV), choline acetyltransferase (ChAT) and SMI312,
195 respectively, on one intact FFPE mouse brain (**Figure 3**). For each round, the brain was labeled not
196 only with the antibody specific for the target protein, but also for lectin as a structural reference. Image
197 datasets from each immunolabeling round were combined into a single multichannel image (**Figure**
198 **4**A), with lectin-labeled blood vessels deployed as a reference channel using Elastix,[54] demonstrating
199 the ability of MOCAT+ to reveal the spatial distribution of different neuronal markers. We conducted

200 a more detailed examination of the habenula-interpeduncular circuitry (Hbn-IPN circuitry) and its
201 connection with these biomarkers. We visualized the expression of ChAT, calbindin, TH, and TPH2
202 in the IPN and the neighboring regions (Figure 4B). Previous studies have shown that these neurons
203 are regulated by the Hbn-IPN circuitry through their connections with the IPN region, which plays a
204 role in controlling emotion, addiction, and the reward process.[55,56] To demonstrate that MOCAT+ can
205 also be applied to human brain FFPE blocks, we performed three consecutive rounds of
206 immunolabeling on a 1-mm-thick FFPE human brain specimen collected surgically from the temporal
207 lobe of a brain tumor patient. For each round, the brain tissue was labeled with GFAP/lectin,
208 SMI312/lectin, or MAP2/lectin, respectively (**Figure 5**A). Labeling homogeneity throughout the entire
209 block was confirmed by imaging at depths of 100, 500 and 900 μm (Figure 5B, S12)

210 **2.5. Application of FFPE-MOCAT to mouse disease models**

211 In disease research, volumetric imaging offers precise microenvironmental information and
212 reveals structural changes that are essential for evaluating injuries and therapeutic effects.[13,35,57] As a
213 first assessment of MOCAT applicability to disease models, we subjected an intact FFPE brain from
214 an astrocytoma mouse model (see Materials and Methods) to the MOCAT pipeline to label tumor cells
215 (ASTS1CI-GFP positive astrocytes) and GFAP-positive astrocytes (**Figure 6**A, C). Accordingly, we
216 could segment GFAP-positive astrocytes surrounding the tumor (Figure 6B, D, and E) and classify
217 them according to their distances from the tumor cells. Statistical analysis (Figure 6F) revealed that
218 nearly half of the GFAP-positive astrocytes were within the tumor, with 63.9% being located near the
219 tumor surface (±200 μm). These results demonstrate that FFPE-MOCAT-derived image datasets can
220 reveal cell distributions and the spatial architecture of disease microenvironments.

221 Next, we employed FFPE mouse brains from a traumatic brain injury (TBI) model to showcase
222 the feasibility of employing MOCAT for 3D quantification of neuronal circuit recovery in disease
223 research. Reduced dopamine levels are known to be a major cause of cognitive impairment after
224 TBI.[58] To assess the impact on dopaminergic neural regeneration across four treatment groups (sham,

225 sMN, aNORO@sMN, and aNORO@sMN+AMF; see Materials and Methods for details), we
226 conducted immunolabeling using anti-TH antibodies (Figure 6G) and compared quantitative changes
227 in the dopaminergic system among these groups. We calculated quantitative ipsilateral-to-contralateral
228 changes for three structural features: striatum volume (Figure 6H), nigrostriatal fiber tract volume
229 (Figure 6I), and the number of dopaminergic cells in the substantia nigra (SN) (Figure 6J). The sham
230 group displayed a decrease (~24%) in the ratio of dopaminergic neurons on the injured side to the
231 uninjured control side (Figure 6K), indicative of dopaminergic system malfunction or imbalance.
232 Treatment with aNORO@sMN rescued this disease phenotype (from 76% to 94%) (Figure 6K), a
233 positive impact on dopamine production and transmission recovery post-TBI.

234 Next, we evaluated the therapeutic effect of aNORO@sMN on angiogenesis. To quantify
235 angiogenesis, we selected three regions of interest around brain injury sites and segmented blood
236 vessels (Figure 6L). The aNORO@sMN treatment group exhibited a substantial increase in blood
237 vessel length, surface area, volume, and branch numbers (244%, 301%, 186%, and 220%, respectively)
238 compared to the sham group (Figure 6M), indicating enhanced angiogenesis. Thus, overall, MOCAT
239 facilitates the 3D quantification critical for assessing neuronal damage and recovery in FFPE
240 specimens.

241 We also performed identical TBI procedures and 3D quantification using the SHIELD protocol
242 and SDS-based electrophoresis for brain clearing and labeling (Figure S13), which resulted in
243 comparable quantitative outcomes compared to those determined for FFPE-MOCAT brains (Figure
244 S14). These results indicate that FFPE-MOCAT recovers biomarker signals as effectively as for freshly
245 processed samples, even after the samples have been subjected to prolonged storage as FFPE blocks.

246 **2.6. MOCAT enables expansion microscopy on thick FFPE samples**

247 Expansion microscopy is a super-resolution microscopy technique that overcomes the limitations
248 of optical diffraction by enlarging biological structures. It is achieved by synthesizing a polymer

249 network within the specimen to anchor protein molecules, causing the specimen to physically expand
250 and enabling analysis of sub-cellular structures.[59,60] It is generally difficult to uniformly expand
251 heavily formaldehyde-fixed specimens, such as FFPE tissues, due to the formaldehyde occupying the
252 binding sites of anchoring reagents. ExPath, a modified version of protein-extension expansion
253 microscopy (ProExM) in which the EDTA concentration in the proteinase K digestion buffer is
254 increased, was developed to overcome this issue.[61] However, although ExPath has been successfully
255 deployed to expand 5-μm-thick FFPE sections, it cannot uniformly expand samples beyond 1 mm even
256 with a prolonged incubation time (**Figure 7**A). We discovered that tissues embedded in paraffin and
257 subjected to the optimized antigen retrieval step in the MOCAT pipeline can be directly expanded
258 using the original ProExM method without extended incubation, yielding clear staining signal for
259 abundant targets such as SMI312 or MAP2 (Figure 7B and C).

260

261 **3. Discussion**

262 In this study, we propose MOCAT, which utilizes a heat-induced antigen retrieval protocol optimized
263 with 1% Tween 20, to eliminate residual lipids and recover masked antigens from FFPE specimens.
264 Our method enables labeling agents to penetrate to a depth of centimeters within such specimens,
265 enabling large-scale neuronal circuitry analyses of archived brain tissues and providing comprehensive
266 information that previously could not typically be obtained from conventional 3-5 μm FFPE sections.
267 We have demonstrated herein that FFPE samples subjected to the MOCAT pipeline can be repeatedly
268 stained without compromising their integrity. Moreover, in evaluating therapeutic efficacy for a TBI
269 mouse model, we found that MOCAT-treated FFPE mouse brains provided as much statistical
270 information as shortly PFA-fixed mouse brains.

271 **3.1. MOCAT facilitates retrospective 3D analyses of neuronal diseases**

272 FFPE processing and sectioning are standard procedures in pathology departments, and FFPE sections
273 are routinely subjected to targeted chemical staining or immunohistochemistry for morphological
274 observations, biomarker validations, or clinical diagnoses.[62,63] However, it is challenging to obtain
275 brain-wide information from conventional 3-5 μm-thick FFPE sections for studies of
276 neurodegenerative diseases.[64] Moreover, biomarker quantifications and structural observations of 2D
277 sections can be biased by sectioning positions and orientations. By applying MOCAT/MOCAT+, 3D
278 histological information can be collected from FFPE specimens, thereby providing more accurate
279 biomarker quantifications, brain-wide neuronal circuitry and cell analyses. Moreover,
280 MOCAT/MOCAT+ may be performed on archived patient samples hosted in neuronal disease brain
281 banks to establish a 3D biomarker atlas for neurological diseases, maximizing the utility of archived
282 specimens. Such an atlas would represent an invaluable resource for retrospective research on
283 biomarker distributions throughout the entire neural network, enabling tracking of their changes and
284 interactions. The resulting comprehensive imaging datasets could also be deployed to train deep
285 learning models, explore potential therapeutic targets, and to predict early diagnostic markers.

286 **3.2. FFPE-MOCAT as an archival and delipidation strategy for clearing centimeter-sized tissue**
287 **samples**

288 The development of tissue clearing has revolutionized neuroscientific research. However, current
289 tissue-clearing protocols impose a 24-hour fixation limit on mouse brains, requiring immediate tissue
290 clearing and labeling upon animal sacrifice. MOCAT offers a solution to this predicament by enabling
291 long-term preservation of mouse brains in FFPE blocks. Accordingly, clinical samples can be
292 conveniently transported to imaging facilities and staining decisions can be postponed until essential
293 analytical results, such as RNA sequencing, become available. Additionally, MOCAT minimizes
294 excessive use of experimental mice in time-course studies by allowing brain samples in FFPE blocks
295 after sacrifice, adhering to 3Rs principles. Consequently, researchers can decide on whole-brain

296 staining approaches upon completing experiments, such as for toxicological or pharmacological targets,
297 thereby avoiding the need to repeat animal experiments.

298 Another possible application of FFPE-MOCAT is to use it as a tissue clearing method for removing
299 lipids. Since paraffin embedding, dewaxing, and heat-induced antigen retrieval are commonly used
300 pathological procedures, FFPE-MOCAT can be quickly, easily, and efficiently executed in the
301 pathology department of hospitals or research institutions, reinforcing its potential utility in clinical
302 research.

303 **3.3. Heating source and buffer choices for heat-induced antigen retrieval in MOCAT**

304 Early efforts to clear and label archived FFPE specimens have only achieved limited labeling depths,
305 [35–40] likely due to a lack of effective antigen retrieval. Protein denaturants employed in hydrophilic
306 tissue clearing protocols, such as SDS (in CLARITY, PACT, FLASH) and urea (in CUBIC and Scale),
307 enhance signal intensity and specificity for some types of specimens, such as cryosections or well-
308 controlled formalin-fixed but non-paraffin-embedded tissues. However, their utility for FFPE tissues
309 is less apparent, with temperature being considered a primary factor in their applicability in such
310 instances.

311 Heat-induced antigen retrieval has been widely used since first being reported by Shi et al. in 1991,
312 with many protocol variations since being developed, including the use of different heat sources (e.g.,
313 water baths, steamers, microwave ovens, autoclaves, and pressure cookers) and buffer choices (low
314 molarity buffers of acid or alkaline pH).[65] Nevertheless, a unifying principle is to heat the fixed tissue
315 sections in buffer solutions at or above 100 °C for up to 30 minutes without boiling.[51,65] In our study,
316 we used a pressure cooker as the heat source to achieve a temperature of ~121 °C, thereby ensuring
317 temperature stability and time efficiency. Any heating condition that is effective for FFPE sections
318 should also work for centimeter-scale FFPE specimens (e.g., using water baths at 95-99 °C), but their
319 effects on delipidation require further testing.

320 The choice of antigen retrieval solutions depends on the antibody being deployed. For example, EDTA
321 solutions are favorable for antibodies against phosphorylated tyrosine.[65,66] Generally, alkaline pH
322 solutions exhibit higher antigen retrieval efficiency, but they are also more tissue-destructive and result
323 in higher background signal compared to lower pH solutions.[41,65] In our study, we tested the addition
324 of 1% Tween 20 to two common antigen retrieval solutions, citrate buffer (pH 6.0) and Tris-EDTA
325 (pH 9.0), both of which yielded satisfactory staining results (Figure S15), demonstrating that MOCAT
326 facilitates the choice between acidic or alkaline antigen retrieval solutions based on antibody
327 preference without compromising the delipidation effect.

328 **3.4 Staining strategies and Epoxy/hydrogel pre-treatments in MOCAT**

329 In Figure 1B, we propose two staining strategies for samples with thicknesses less than 500 um and
330 greater than 1 mm: passive immunolabeling and active immunolabeling. In passive immunolabeling,
331 antibodies penetrate and reach their targets solely through diffusion, without any additional force. It
332 takes approximately two months to passively stain a whole mouse brain.[26,28] Compared to passive
333 immunolabeling, active immunolabeling uses an external force, such as pressure, electrophoresis, etc.,
334 to facilitate antibody penetration and therefore significantly speed up the staining process, reducing
335 the required staining time for a whole mouse brain to one day. However, the harsh conditions, such as
336 pressure and heat, caused by external forces might damage specimens. To protect specimens from the
337 harsh conditions caused by active staining, specimens could be strengthened by treatment with epoxy
338 or acrylamide monomer to form a tissue-epoxy or tissue-hydrogel hybrid.[29,31] Laboratories that do
339 not have adequate devices or handle small specimens could use passive immunolabeling instead and
340 skip the step of epoxy or hydrogel pretreatment.

341 **3.5. Limitations**

342 We acknowledge that there are some limitations to MOCAT application, which we wish to address.
343 Firstly, the FFPE tissues we tested in this study have been limited to mouse and human brain tissues

344 fixed under well-controlled conditions. Differences in tissue fixation procedures at different hospitals
345 and tissue banks may affect the clarity and immunostaining efficiency of dewaxed FFPE tissues. In
346 the demonstration of MOCAT to 3-month fixed specimens, we observed that pontine reticular nucleus
347 (Figure S6A, yellow arrowheads) lose TH-positive signals after long-term fixation. The fluorescence
348 intensity was more affected by fixation with formalin, which is methanol-stabilized and stronger, than
349 with PFA. The results indicate that a stronger antigen retrieval method may be a possible solution.
350 However, achieving the right balance between antigen retrieval efficiency and tissue integrity will
351 require additional testing and investigation. Secondly, MOCAT has not yet been extensively tested on
352 tissues other than the brain. Thus, its applicability and effectiveness for other tissues remain to be
353 established. Third, the size of the samples used in this study is mostly in the range of 2-3 cm^3. Larger
354 samples may require a prolonged incubation time and/or increased Tween 20 concentration. Fourth,
355 MOCAT is not compatible with endogenous fluorescence due to a reduction in fluorescence intensity
356 caused by xylene and alcohol used in paraffin processing. Researchers who need to directly observe
357 genetically encoded fluorescent proteins can utilize tissue-clearing methods such as 3DISCO, X-
358 CLARITY, CUBIC, etc., which have been shown to minimize the decrease in fluorescence intensity.
359 On the other hand, if researchers need to visualize transgenic fluorescent proteins along with other
360 biomarkers, they can use MOCAT for delipidation and boost-immunolabeling to visualize the
361 transgenic fluorescent proteins. Fifth, MOCAT+ may not be suitable for cases necessitating iterative
362 staining with the same antibody. In addition, the applicability of MOCAT+ to antibodies not tested in
363 the study requires further testing and validation. Finally, whether MOCAT-treated tissues retain
364 sufficient molecular features and structural integrity for omics analysis warrants verification. Further
365 research and testing will help to address these limitations and improve the applicability and
366 effectiveness of the MOCAT pipeline we present herein.

367

368 **4. Conclusions**

369 In conclusion, as a method enabling multi-round immunolabeling of centimeter-scale archived FFPE
370 specimens, MOCAT/MOCAT+ presents new possibilities for researching neural disease and could
371 serve as a powerful tool for neuronal circuitry analyses and pathology. Its integration with conventional
372 pathological procedures also renders it readily applicable in clinical settings. Through further
373 validation across various organs and testing of its compatibility with spatial omics techniques,
374 MOCAT could potentially catalyze broader and more comprehensive investigations in both the
375 fundamental and clinical research domains.

376 **Materials and Methods**

377 *Experimental animals and human samples*

378 We used 8-week-old CD-1 male mice to develop the MOCAT pipeline. All animal procedures and
379 handling complied with guidelines from the Institutional Animal Care and Use Committee of
380 Academia Sinica (IACUC protocol No.: 12-05-370), Taiwan. Information on the astrocytoma and TBI
381 mouse models is provided in the respective subsections below. The analyses involving human
382 participants were reviewed and approved by the Institutional Review Board of National Taiwan
383 University Hospital (IRB No.: 202203079RINC), and all participants provided signed informed
384 consent.

385 *Astrocytoma animal model*

386 All animal procedures and handling complied with guidelines from the Institutional Animal Care and
387 Use Committee of National Tsing Hua University (IACUC protocol No.: 109067), Taiwan. ALTS1C1-
388 GFP cells (1×10^5 cells) were implanted into the brains of 8-week-old C57BL/6 mice according to a
389 previously published procedure.[67] In brief, 1×10^5 ALTS1C1-GFP cells were injected into the
390 C57BL/6 mice under anesthesia at a depth of 2.5 mm and 2 mm lateral to the midline and 1 mm
391 posterior to the bregma. After injection, bone wax (ETHICON, W810, Somerville, NJ, USA) was
392 applied to seal the drilled hole. Eighteen days after tumor implantation, mice were sacrificed after
393 cardiac perfusion.

394 *TBI mouse model*

395 All animal procedures and handling complied with guidelines from the Institutional Animal Care and
396 Use Committee of National Tsing Hua University (IACUC protocol Number: 110081). We divided 7-
397 week-old C57BL/6 female mice into four groups: (1) untreated (sham), (2) treated with a paracetamol-
398 coated silk-based microneedle (sMN), (3) treated with alternating magnetic field-responsive NO-
399 release octahedrons (aNORO@sMN), and (4) treated with aNORO@sMN and an alternating magnetic
400 field (aNORO@sMN+AMF). To perform traumatic brain injury (TBI), we used an electric drill to

401 create a hole in the skull at the left motor cortex (M1 & M2) and used a 2-mm-diameter punch to cause
402 a 1.5-mm-deep injury. For all treatments except sham, the microneedle was implanted one day post-
403 injury to avoid excessive swelling in the injured area. For the aNORO@sMN and
404 aNORO@sMN+AMF groups, the NO-release octahedrons (aNORO) were embedded in a silk
405 microneedle (sMN). For the AMF-treated group, a magnetic field at a power of 3.2 kW and a frequency
406 of 1 MHz was applied for 5 min per day until the mice were sacrificed. Additional experimental details
407 are as described in Chan et al..[68] Mice were sacrificed 45 days after TBI induction.

408 *Sample collection and preparation*

409 For mouse brain samples, the mice were euthanized by injecting them with 0.2 mL of a 30% Urethane
410 saline solution. The euthanized mice were perfused with 20 mL of cold phosphate-buffered saline
411 (PBS) and 20 mL of 4% PFA. The collected brains were further fixed using 4% PFA at 4 °C for 24
412 hours. Human brain tissue specimens were surgically collected from the temporal lobe of patients and
413 fixed with 4% PFA at 4 °C for 24 hours. For paraffin embedding, fixed specimens were dehydrated
414 and processed in a tissue processor (Tissue-Tek VIP 5 Jr., Sakura Finetek Japan Co. Ltd., Japan) under
415 vacuum conditions and then embedded in paraffin wax.

416 *SHIELD processing, SDS-electrophoretic delipidation and FLASH delipidation*

417 PFA-fixed specimens were incubated in SHIELD-OFF solution at 4 °C for 96 hours, followed by
418 incubation for 24 hours in SHIELD-ON solution at 37 °C. All reagents were prepared using SHIELD
419 kits (LifeCanvas Technologies, Seoul, South Korea) according to the manufacturer's instructions. For
420 SDS-electrophoretic delipidation, SHIELD-processed specimens were placed in a stochastic electro-
421 transport machine (SmartClear Pro II, LifeCanvas Technologies, Seoul, South Korea) running at a
422 constant current of 1.2 A for 5-7 days. For FLASH delipidation, the SHIELD-processed specimens
423 were placed in FLASH reagent (4% w/v SDS, 200 mM borate) and then incubated at 54 °C for 18
424 hours.[47] The delipidated specimens were washed with PBST at room temperature for at least 1 day.

425 *Evaluating the extent of delipidation*

426 Serial 20-μm-thick cryosections were cut from mouse brain slices (2-mm thick) of various treatment
427 conditions for subsequent DiD or Oil red O staining. For DiD staining, cryosections (that were of
428 approximately 0-40 μm depth) were post-fixed with 4% PFA at room temperature for 5 minutes. The
429 sections were then rinsed with distilled water and immersed in PBST (PBS with 0.1% Triton X-100)
430 for 10 minutes to remove OCT. These sections were stained with 0.0025 uM DiD/PBST solution at
431 room temperature for 1 hour, before rinsing them with distilled water and washing with 1% SDS for
432 several seconds to remove excess DiD. The slides were mounted in 50% glycerol and imaged under a
433 Zeiss 780 confocal microscope using a 10× 0.75NA Plan-Apochromat objective (Zeiss). For Oil red
434 O staining, the sections (that were of approximately 40-80 μm depth) were post-fixed with a 4%
435 formal-calcium solution for 5 minutes and then rinsed with distilled water. The fixed sections were
436 pre-incubated in 60% isopropanol for 5 minutes and then stained with fresh Oil red O working solution
437 (0.3% Oil red O in 60% isopropanol) for 15 minutes. The sections were briefly washed with 60%
438 isopropanol and mounted in glycerine jelly. Images were acquired using a 3DHISTECH Pannoramic
439 250 slide scanner with a 40× 0.95NA Plan-Apochromat objective (Zeiss). Details of statistical analyses
440 are described in the *Quantification and Statistics* section below.

441 *Comparison of brain region volume*

442 Autofluorescence-channel imaging datasets of whole mouse brains were aligned to the BrainGlobe
443 Atlas API[53] using the aMAP tool.[69] The volume of each brain subregion was then obtained and
444 organized based on anatomical hierarchy using the Allen Brain Atlas. The 679 subregions were merged
445 into 78 brain regions at the same anatomical hierarchy as the hippocampus. The brain region volume
446 of right and left hemisphere of the FFPE-MOCAT mouse brain was compared and plotted using
447 GraphPad Prism 9.5.1 (GraphPad Software Inc., San Diego, CA, USA).

448 *MOCAT pipeline*

449 The MOCAT pipeline is illustrated in Figure 1C and described in detail below.

450 *Deparaffination and rehydration*. FFPE blocks were incubated at 65-70 °C to melt the paraffin.
451 Residual paraffin was removed through immersion in xylene for 24 hours, with the xylene being
452 changed at least twice. Dewaxed brains were rehydrated with 100%, 100%, 95%, 85%, 75%, and 55%
453 alcohol diluted with distilled water. The rehydrated brains were then washed with PBS.

454 *Epoxy processing*. Specimens were processed with commercialized SHIELD kit as described above.

455 *Optimized antigen retrieval*.

456 Specimens were incubated overnight at 37 °C in a modified citrate buffer (10 mM sodium citrate, 1%
457 Tween 20, pH 6.0). The specimens and buffer were then heated for 10 minutes at 121 °C in a pressure
458 cooker (Bio SB, Santa Barbara, CA, USA) and kept in the pressure cooker until the temperature
459 dropped below 100 °C (for approximately 15 minutes). Next, the specimens were removed from the
460 cooker and cooled for 10 minutes at room temperature. The specimens were then washed three times
461 in PBST, with each wash lasting 1 hour.

462 *Electrophoretic immunolabeling (active staining)*. The procedure was modified from the previously
463 published eFLASH protocol[15] and was conducted in a SmartLabel System (LifeCanvas Technologies,
464 Seoul, South Korea). The specimens were preincubated overnight at room temperature in sample
465 buffer (240 mM Tris, 160 mM CAPS, 20% w/v D-sorbitol, 0.9% w/v sodium deoxycholate). Each
466 preincubated specimen was placed in a sample cup (provided by the manufacturer with the SmartLabel
467 System) containing primary, corresponding secondary antibodies and lectin diluted in 8 mL of sample
468 buffer. Information on antibodies, lectin and their optimized quantities is detailed in Supplementary
469 Table 1. The specimens in the sample cup and 500 mL of labeling buffer (240 mM Tris, 160 mM
470 CAPS, 20% w/v D-sorbitol, 0.2% w/v sodium deoxycholate) were loaded into the SmartLabel System.
471 The device was operated at a constant voltage of 90 V with a current limit of 400 mA. After 18 hours
472 of electrophoresis, 300 mL of booster solution (20% w/v D-sorbitol, 60 mM boric acid) was added,
473 and electrophoresis continued for 4 hours. During the labeling, the temperature inside the device was
474 kept at 25 °C. Labeled specimens were washed twice (3 hours per wash) with PTwH (1× PBS with

475 0.2% w/v Tween-20 and 10 μg/mL heparin),[23] and then post-fixed with 4% PFA at room temperature
476 for 1 day. Post-fixed specimens were washed twice (3 hours per wash) with PBST to remove any
477 residual PFA.

478 *Refractive index (RI) matching*. Before imaging, the specimens were RI-matched by immersing them
479 in NFC1 (RI = 1.47) and NFC2 (RI = 1.52) solutions (Nebulum, Taipei, Taiwan) at room temperature
480 for 1 day for each solution.

481 *Volumetric imaging and 3D visualization*. For centimeter-scale specimens, images were acquired using
482 a light-sheet microscope (SmartSPIM, LifeCanvas Technologies, Seoul, South Korea) with a 3.6x
483 customized immersion objective (NA = 0.2, working distance = 1.2 cm). For samples <3 mm thick,
484 imaging was performed using a multipoint confocal microscope (Andor Dragonfly 200, Oxford
485 Instruments, UK) with objectives that were UMPLFLN10XW (10x, NA = 0.3, working distance = 3.5
486 mm), UMPLFLN20XW (20x, NA = 0.5, working distance = 3.5 mm), UMPLFLN40XW (40x, NA =
487 0.8, working distance = 3.3 mm). 3D visualization was performed using Imaris software (Imaris 9.5.0,
488 Bitplane, Belfast, UK).

489 *Photobleaching*. Immunolabeled and imaged specimens were placed in a multi-well plate and
490 immersed in RI-matching solutions so they retained transparency. The plate was then sealed with
491 paraffin. A 100-W projection lamp with an LED array was placed on the plate to quench fluorescence
492 signals. A representative photobleaching apparatus constructed using off-the-shelf components is
493 shown in Supplementary Figure 10a. In our experience, approximately 18 hours photobleaching is
494 sufficient for a 2-mm-thick sample, whereas 3 days is required for a whole mouse brain (approximately
495 8 mm to 1 cm in thickness).

496 *Raman microscopy*

497 A Yb:KGW laser (Carbide, Light Conversion) emitting a 190 fs, 200 kHz, 20 W pulse train at a 1030
498 nm wavelength was used to generate a supercontinuum via a double-pass multiple-plate continuum
499 module. The resulting spectrum (600-1300 nm) was spectrally sliced by tunable color filters (3G

500 LVLWP, LVSWP, and LVFBP, Delta) to provide pump (725 nm) and Stokes (914 nm) beams, which
501 could address the Raman shift (2850 cm-1) of lipids. The two beams were temporally and spatially
502 overlapped, and then guided into a commercial upright microscope (Axio Examiner.Z1, Zeiss) with a
503 scanning unit (LSM7MP, Zeiss) to achieve raster scanning on the x-y plane. A single 20x water
504 immersion objective (UMPLFLN 20XW, Olympus) was used to focus the combined laser beams on
505 the mouse sample. Epi-CARS signal at 601 nm was spectrally separated from the incident radiation
506 with a bandpass filter (BP 565-610, Zeiss) and detected using a photomultiplier tube.

507 *Multichannel image registration*

508 For six-round immunolabeling of a single whole mouse brain, each dataset included one structural
509 reference channel stained with lectin and one antibody-stained channel. The first round of staining
510 served as the standard brain, with lectin channel images of each subsequent dataset being registered to
511 the lectin channel of the standard brain using the Elastix toolbox.[54] The transformation parameters
512 obtained from rigid and B-spline deformable registration of the lectin channels were then applied to
513 the antibody-stained channels. The transformed images were merged and visualized using Imaris
514 software. In the case of three-round immunolabeling of human specimens, the image datasets from the
515 three rounds were registered and resampled using Amira software (Thermo Fisher Scientific, Waltham,
516 MA, USA), and then merged and visualized using Imaris software.

517 *Expansion microscopy and ExPath*

518 Expansion microscopy was performed using the proExM protocol.[58] A 1-mm-thick MOCAT-
519 processed FFPE mouse brain slice was incubated in anchoring solution (0.01% w/v methacrylic acid
520 N-hydroxysuccinimide ester in 1×PBS) at 4 °C for 24 hours. After anchoring, the sample was washed
521 twice (5 minutes each time) with PBS at room temperature and then rinsed twice (5 minutes each time)
522 in acrylamide monomer solution (2 M NaCl, 8.625% w/w sodium acrylate, 2.5% w/w acrylamide,
523 0.15% w/w N,N'-methylene-bisacrylamide in 1×PBS) at 4 °C. For gelation, the specimen was pre-
524 incubated in gelation solution (0.02% w/w ammonium persulfate (APS), 0.02% w/w tetramethyl-

525 ethylenediamine (TEMED), and 0.01% w/w 4-hydroxy-2,2,6,6-tetramethylpiperidin-1-oxyl (4-
526 hydroxy-TEMPO) in monomer solution) for 5 minutes at 4 °C, and then moved into fresh gelation
527 solution for an additional 25 minutes. The specimen in gelation solution was then transferred to a
528 humidified 37 °C incubator for 2 hours. The gel was then immersed in a digestion solution (8 units/ml
529 proteinase K, 50 mM Tris, 1 mM EDTA, 0.5% w/v Triton X-100, 1M NaCl, pH 8.0) at 37 °C for 4
530 hours. After digestion, the gel was immersed in an excess of deionized water for 0.5-2 hours to expand.
531 This step was repeated 3−5 times with fresh water until the size of the sample ceased to increase.

532 For the ExPath experiment, a 1-mm-thick FFPE mouse slice was dewaxed, rehydrated and underwent
533 the same anchoring and gelation steps as described above. The gel was digested in ExPath digestion
534 solution (8 units/ml proteinase K, 50 mM Tris, 25 mM EDTA, 0.5% w/v Triton X-100, 0.8M NaCl,
535 pH 8.0) at 60 °C for 3 hours.[59]

536 *Post-expansion immunolabeling*

537 Digested gels were washed twice (20 minutes each time) in PBS, and then incubated in a primary
538 antibody cocktail containing anti-SMI312 (Biolegend, 837904, 1:500 dilution), anti-MAP2 (Cell
539 Signaling Technology, #8707, 1:500 dilution), 2% v/v normal goat serum (Jackson ImmunoResearch,
540 005-000-121, 1:500 dilution), and 0.1% w/v Triton X-100 in 1×PBS at 4 °C for 24 hours. The gels
541 were then washed three times (20 minutes each time) in wash buffer (30 mM sodium chloride, 0.1%
542 w/v Triton X-100 in 1×PBS) and incubated in a secondary antibody cocktail containing Alexa Fluor®
543 647 AffiniPure goat anti-mouse IgG (Jackson ImmunoResearch, 115-605-003, 1:500 dilution),
544 Rhodamine Red™-X (RRX) AffiniPure goat anti-rabbit IgG (Jackson ImmunoResearch, 111-295-003,
545 1:500 dilution), 0.2% v/v normal goat serum, and 0.1% w/v Triton X-100 in 1×PBS at 4 °C for 24
546 hours. The antibody-labeled gels were washed three times (20 minutes each time) in wash buffer and
547 then placed in deionized water for expansion. For nuclei staining, propidium iodine was added to
548 deionized water at a final concentration of 1 μg/ml during expansion.

549 *Quantification and statistics*

550 To quantify the extent of delipidation (Figure 1A), DiD-stained sections were imaged at an excitation
551 wavelength of 642 nm. To quantify the fluorescence intensity, 10 regions of interest (ROI) of 0.8 × 0.8
552 mm were selected randomly within the cortex of each specimen. The gray (pixel) value of each ROI
553 was measured using Fiji,[70] Mean values and standard deviations (SD) were plotted using GraphPad
554 Prism 9.5.1 (GraphPad Software Inc., San Diego, CA, USA). The significance of the difference in
555 mean values was determined by means of one-way ANOVA with Tukey's multiple comparison tests
556 at an α level = 0.05 (*P < 0.05; **P < 0.01; ***P < 0.001; ****P < 0.0001).

557 For the Raman signal quantification shown in Figure 1F, gray values of 18 Raman images (0.4 × 0.4
558 mm) at a different depth for each group were measured using Fiji. The mean values and SD were
559 determined, and the significance of differences were also calculated by means of one-way ANOVA
560 using GraphPad Prism as described above.

561 For the astrocyte-tumor distance analysis shown in Figure 6F, the astrocytes were segmented using the
562 SPOT module of Imaris based on a fluorecence intensity threshold and point spread function (PSF)
563 size definition. GFP-expressing tumors were segmented using the Surface module of Imaris. Distances
564 of all segments were calculated in Imaris.

565 To quantify dopaminergic regions in TBI mouse brains, the volume of the striatum and nigrostriatal
566 fiber tracts was calculated using the Surface module of Imaris, and cell number in the substantia nigra
567 was determined using the SPOT module. To demonstrate the similarity of quantification results from
568 FFPE-MOCAT and PFA-SDS brains, the quantification data for the injured side of each brain was
569 normalized according to the results for the corresponding contralateral side. Mean values and SD were
570 plotted using GraphPad Prism (N = 3 in Figure 6K and Supplementary Figure 9a). The significance of
571 the difference in mean values was determined by means of one-way ANOVA with Tukey's multiple
572 comparison tests at an α level = 0.05 (*P < 0.05; **P < 0.01; ***P < 0.001; ****P < 0.0001).

573 To evaluate angiogenesis, we selected three ROIs (each of 0.6 × 0.6 × 0.6 mm) close to the injury site.
574 The Surface module of Imaris was used to segment the blood vessels and calculate their total volume

575 and surface area. Their length and numbers of bifurcation points were calculated using Vessap.[71]
576 Erosion and dilation were performed to remove false-negative pixels and to avoid false centerline
577 detections. Next, the centerlines were extracted by means of a 3D thinning algorithm.[72] The
578 bifurcation points were detected using the surrounding pixels of each point to define a point that splits
579 into two or more vessels. Mean values, SD, and the significance of differences were calculated by
580 independent *t* test using GraphPad Prism.

Acknowledgements

We thank the Brain Research Center, National Tsing-Hua University, Taiwan and Pathology core, Institute of Biomedical Sciences, Academia Sinica, Taiwan for the technical assistance. This work was funded by the grants from National Science and Technology Council (NSTC-111-2636-B-007-007, NSTC-07-2314-B-007-003-MY3, NSTC-111-2321-B-002-016, MOST-110-2321-B-010-006). This work was also supported by the Brain Research Center under the Higher Education Sprout Project, co-funded by the Ministry of Education and the National Science and Technology Council in Taiwan.

Conflict of Interest

The authors declare no conflict of interest.

Data Availability Statement

The raw data that support the findings of this study are available upon request.

References

1. Rajput, A. H. & Rajput, A. Saskatchewan Movement Disorders Program. *Can. J. Neurol. Sci.* **42**, 74–87 (2015).

2. Hernandez-Ronquillo, L. *et al.* The Concept of an Epilepsy Brain Bank. *Front. Neurol.* **11**, 553157 (2020).

3. Latimer, C. S. *et al.* Protocol for the Systematic Fixation, Circuit-Based Sampling, and Qualitative and Quantitative Neuropathological Analysis of Human Brain Tissue. *Methods Mol. Biol.* **2561**, 3–30 (2023).

4. Talari, K. & Goyal, M. Retrospective Studies – Utility and Caveats. *https://doi.org/10.4997/jrcpe.2020.409* **50**, 398–402 (2020).

5. Jacobsen, S. B., Tfelt-Hansen, J., Smerup, M. H., Andersen, J. D. & Morling, N. Comparison of whole transcriptome sequencing of fresh, frozen, and formalin-fixed, paraffin-embedded cardiac tissue. *PLoS One* **18**, e0283159 (2023).

6. Zhao, L. *et al.* FACT-seq: profiling histone modifications in formalin-fixed paraffin-embedded samples with low cell numbers. *Nucleic Acids Res.* **49**, e125–e125 (2021).

7. Zhong, J. *et al.* Enhanced and controlled chromatin extraction from FFPE tissues and the application to ChIP-seq. *BMC Genomics* **20**, 1–11 (2019).

8. Fraggetta, F. *et al.* The Importance of eSlide Macro Images for Primary Diagnosis with Whole Slide Imaging. *J. Pathol. Inform.* **9**, 46–46 (2018).

9. Kumar, N., Gupta, R. & Gupta, S. Whole Slide Imaging (WSI) in Pathology: Current Perspectives and Future Directions. *J. Digit. Imaging* **33**, 1034–1040 (2020).

10. Patel, A. *et al.* Contemporary Whole Slide Imaging Devices and Their Applications within the Modern Pathology Department: A Selected Hardware Review. *J. Pathol. Inform.* **12**, 50 (2021).

11. Richardson, D. S. & Lichtman, J. W. Clarifying Tissue Clearing. *Cell* **162**, 246–257 (2015).

12. Ueda, H. R. *et al.* Tissue clearing and its applications in neuroscience. *Nature Reviews Neuroscience* vol. 21 61–79 (2020).

13. Gómez-Gaviro, M. V., Sanderson, D., Ripoll, J. & Desco, M. Biomedical applications of tissue clearing and three-dimensional imaging in health and disease. *iScience* **23**, 101432 (2020).

14. Richardson, D. S. *et al.* TISSUE CLEARING. *Nat. Rev. Methods Prim.* **1**, (2021).

15. Yun, D. H. *et al.* Ultrafast immunostaining of organ-scale tissues for scalable proteomic phenotyping. *bioRxiv* 660373 (2019) doi:10.1101/660373.

16. Susaki, E. A. *et al.* Versatile whole-organ/body staining and imaging based on electrolyte-gel properties of biological tissues. *Nat. Commun. 2020 111* **11**, 1–22 (2020).

17. Yau, C. N. *et al.* Principles of deep immunohistochemistry for 3D histology. (2023) doi:10.1016/j.crmeth.2023.100458.

18. Conchello, J. A. & Lichtman, J. W. Optical sectioning microscopy. *Nat. Methods 2005 212* **2**, 920–931 (2005).

19. Dodt, H. U. *et al.* Ultramicroscopy: Three-dimensional visualization of neuronal networks in the whole mouse brain. *Nat. Methods* **4**, 331–336 (2007).

20. Reynaud, E. G., Kržič, U., Greger, K. & Stelzer, E. H. K. Light sheet-based fluorescence microscopy: More dimensions, more photons, and less photodamage. *HFSP J.* **2**, 266–275 (2008).

21. Yu, T., Zhu, J., Li, D. & Zhu, D. Physical and chemical mechanisms of tissue optical clearing. *iScience* **24**, 102178 (2021).

22. Ertürk, A. *et al.* Three-dimensional imaging of solvent-cleared organs using 3DISCO. *Nat. Protoc.* **7**, 1983–1995 (2012).

23. Renier, N. *et al.* IDISCO: A simple, rapid method to immunolabel large tissue samples for volume imaging. *Cell* **159**, 896–910 (2014).

24. Jing, D. *et al.* Tissue clearing of both hard and soft tissue organs with the pegasos method. *Cell Res.* **28**, 803–818 (2018).

25. Hama, H. *et al.* Scale: a chemical approach for fluorescence imaging and reconstruction of transparent mouse brain. *Nat. Neurosci. 2011 1411* **14**, 1481–1488 (2011).

26. Susaki, E. A. *et al.* Whole-brain imaging with single-cell resolution using chemical cocktails and computational analysis. *Cell* **157**, 726–739 (2014).

27. Hama, H. *et al.* ScaleS: An optical clearing palette for biological imaging. *Nat. Neurosci.* **18**, 1518–1529 (2015).

28. Tainaka, K. *et al.* Chemical Landscape for Tissue Clearing Based on Hydrophilic Reagents. *Cell Rep.* **24**, 2196-2210.e9 (2018).

29. Chung, K. *et al.* Structural and molecular interrogation of intact biological systems. *Nature* **497**, 332–337 (2013).

30. Murray, E. *et al.* Simple, Scalable Proteomic Imaging for High-Dimensional Profiling of Intact Systems. *Cell* **163**, 1500–1514 (2015).

31. Park, Y.-G. *et al.* Protection of tissue physicochemical properties using polyfunctional crosslinkers. *Nat. Biotechnol.* **37**, 73–83 (2019).

32. Cai, R. *et al.* Panoptic imaging of transparent mice reveals whole-body neuronal projections and skull–meninges connections. *Nat. Neurosci.* **22**, 317–327 (2019).

33. Mai, H. *et al.* Whole-body cellular mapping in mouse using standard IgG antibodies. *Nat. Biotechnol. 2023* 1–11 (2023) doi:10.1038/s41587-023-01846-0.

34. Zhao, S. *et al.* Cellular and Molecular Probing of Intact Human Organs. *Cell* **180**, 796-812.e19 (2020).

35. Chen, Y. *et al.* Three-dimensional imaging and quantitative analysis in CLARITY processed breast cancer tissues. *Sci. Rep.* **9**, 1–13 (2019).

36. Hughes, C., Gaunt, L., Brown, M., Clarke, N. W. & Gardner, P. Assessment of paraffin removal from prostate FFPE sections using transmission mode FTIR-FPA imaging. *Anal. Methods* **6**, 1028–1035 (2014).

37. Lai, H. M. *et al.* Next generation histology methods for three-dimensional imaging of fresh and archival human brain tissues. *Nat. Commun. 2018 91* **9**, 1–12 (2018).

38. Nojima, S. *et al.* CUBIC pathology: Three-dimensional imaging for pathological diagnosis. *Sci. Rep.* **7**, 1–14 (2017).

39. Tanaka, N. *et al.* Whole-tissue biopsy phenotyping of three-dimensional tumours reveals patterns of cancer heterogeneity. *Nat. Biomed. Eng.* **1**, 796–806 (2017).

40. Tanaka, N. *et al.* Mapping of the three-dimensional lymphatic microvasculature in bladder tumours using light-sheet microscopy. *Br. J. Cancer 2018 1187* **118**, 995–999 (2018).

41. Shi, S.-R., Cote, R. J. & Taylor, C. R. Antigen Retrieval Techniques: Current Perspectives. *J. Histochem. Cytochem.* **49**, 931–937 (2001).

42. Thavarajah, R., Mudimbaimannar, V. K., Elizabeth, J., Rao, U. K. & Ranganathan, K. Chemical and physical basics of routine formaldehyde fixation. *J. Oral Maxillofac. Pathol.* **16**, 400 (2012).

43. Denti, V. *et al.* Antigen Retrieval and Its Effect on the MALDI-MSI of Lipids in Formalin-Fixed Paraffin-Embedded Tissue. *J. Am. Soc. Mass Spectrom.* **31**, 1619–1624 (2020).

44. Robinson, J. M. & Vandré, D. D. Antigen retrieval in cells and tissues: Enhancement with sodium dodecyl sulfate. *Histochem. Cell Biol.* **116**, 119–130 (2001).

45. Brown, D. *et al.* Antigen retrieval in cryostat tissue sections and cultured cells by treatment with sodium dodecyl sulfate (SDS). *Histochem. Cell Biol.* **105**, 261–267 (1996).

46. Woelfle, S. *et al.* CLARITY increases sensitivity and specificity of fluorescence immunostaining in long-term archived human brain tissue. *BMC Biol.* **21**, 1–28 (2023).

47. Messal, H. A. *et al.* Antigen retrieval and clearing for whole-organ immunofluorescence by FLASH. *Nat. Protoc.* **16**, 239–262 (2021).

48. Kim, S. W., Roh, J. & Park, C. S. Immunohistochemistry for Pathologists: Protocols, Pitfalls, and Tips. *J. Pathol. Transl. Med.* **50**, 411 (2016).

49. Shi, S. R., Key, M. E. & Kalra, K. L. Antigen retrieval in formalin-fixed, paraffin-embedded tissues: an enhancement method for immunohistochemical staining based on microwave oven heating of tissue sections. *J. Histochem. Cytochem.* **39**, 741–748 (1991).

50. Norton, A. J., Jordan, S. & Yeomans, P. Brief, high-temperature heat denaturation (pressure cooking): A simple and effective method of antigen retrieval for routinely processed tissues. *J. Pathol.* **173**, 371–379 (1994).

51. Taylor, C. R. *et al.* Comparative study of antigen retrieval heating methods: microwave, microwave and pressure cooker, autoclave, and steamer. *Biotech. Histochem.* **71**, 263–270 (1996).

52. Na, M. *et al.* Sodium Cholate-Based Active Delipidation for Rapid and Efficient Clearing and Immunostaining of Deep Biological Samples. *Small Methods* **6**, (2022).

53. Claudi, F. *et al.* BrainGlobe Atlas API: a common interface for neuroanatomical atlases. *J. Open Source Softw.* **5**, 2668 (2020).

54. Klein, S., Staring, M., Murphy, K., Viergever, M. A. & Pluim, J. P. W. elastix: a toolbox for intensity-based medical image registration. *IEEE Trans. Med. Imaging* **29**, 196–205 (2010).

55. McLaughlin, I., Dani, J. A. & DeBiasi, M. The medial habenula and interpeduncular nucleus circuitry is critical in addiction, anxiety, and mood regulation. *J. Neurochem.* **142**, 130–143 (2017).

56. Fakhoury, M. The dorsal diencephalic conduction system in reward processing: Spotlight on the anatomy and functions of the habenular complex. *Behav. Brain Res.* **348**, 115–126 (2018).

57. Liebmann, T. *et al.* Three-Dimensional Study of Alzheimer's Disease Hallmarks Using the iDISCO Clearing Method. *Cell Rep.* **16**, 1138–1152 (2016).

58. Jenkins, P. O. *et al.* Dopaminergic abnormalities following traumatic brain injury. *Brain* **141**, 797–810 (2018).

59. Chen, F., Tillberg, P. W. & Boyden, E. S. Expansion microscopy. *Science (80-.).* **347**, 543–548 (2015).

60. Tillberg, P. W. *et al.* Protein-retention expansion microscopy of cells and tissues labeled using standard fluorescent proteins and antibodies. *Nat. Biotechnol.* **34**, 987–992 (2016).

61. Zhao, Y. *et al.* Nanoscale imaging of clinical specimens using pathology-optimized expansion microscopy. *Nat. Biotechnol. 2017 358* **35**, 757–764 (2017).

62. Berg, D., Malinowsky, K., Reischauer, B., Wolff, C. & Becker, K. F. Use of formalin-fixed and paraffin-embedded tissues for diagnosis and therapy in routine clinical settings. *Methods Mol. Biol.* **785**, 109–122 (2011).

63. Steeghs, E. M. P. *et al.* Comprehensive routine diagnostic screening to identify predictive mutations, gene amplifications, and microsatellite instability in FFPE tumor material. *BMC Cancer* **20**, 1–15 (2020).

64. Golub, V. M. *et al.* Neurostereology protocol for unbiased quantification of neuronal injury and neurodegeneration. *Front. Aging Neurosci.* **7**, 158767 (2015).

65. Krenacs, L., Krenacs, T., Stelkovics, E. & Raffeld, M. Heat-Induced Antigen Retrieval for Immunohistochemical Reactions in Routinely Processed Paraffin Sections. *Methods Mol. Biol.* **588**, 103 (2010).

66. Pileri, S. A. *et al.* Antigen retrieval techniques in immunohistochemistry: comparison of different methods. *J. Pathol* **183**, 116–123 (1997).

67. Wang, S. C., Hong, J. H., Hsueh, C. & Chiang, C. S. Tumor-secreted SDF-1 promotes glioma invasiveness and TAM tropism toward hypoxia in a murine astrocytoma model. *Lab. Invest.* **92**, 151–162 (2012).

68. Chan, Y. C. *et al.* In situ magnetoelectric generation of nitric oxide and electric stimulus for nerve therapy by wireless chargeable molybdenum carbide octahedrons. *Nano Today* **51**, 101935 (2023).

69. Niedworok, C. J. *et al.* aMAP is a validated pipeline for registration and segmentation of high-resolution mouse brain data. *Nat. Commun. 2016 71* **7**, 1–9 (2016).

70. Schindelin, J. *et al.* Fiji: an open-source platform for biological-image analysis. *Nat. Methods 2012 97* **9**, 676–682 (2012).

71. Todorov, M. I. *et al.* Machine learning analysis of whole mouse brain vasculature. *Nat. Methods 2020 174* **17**, 442–449 (2020).

72. Lee, T. C., Kashyap, R. L. & Chu, C. N. Building Skeleton Models via 3-D Medial Surface Axis Thinning Algorithms. *CVGIP Graph. Model. Image Process.* **56**, 462–478 (1994).

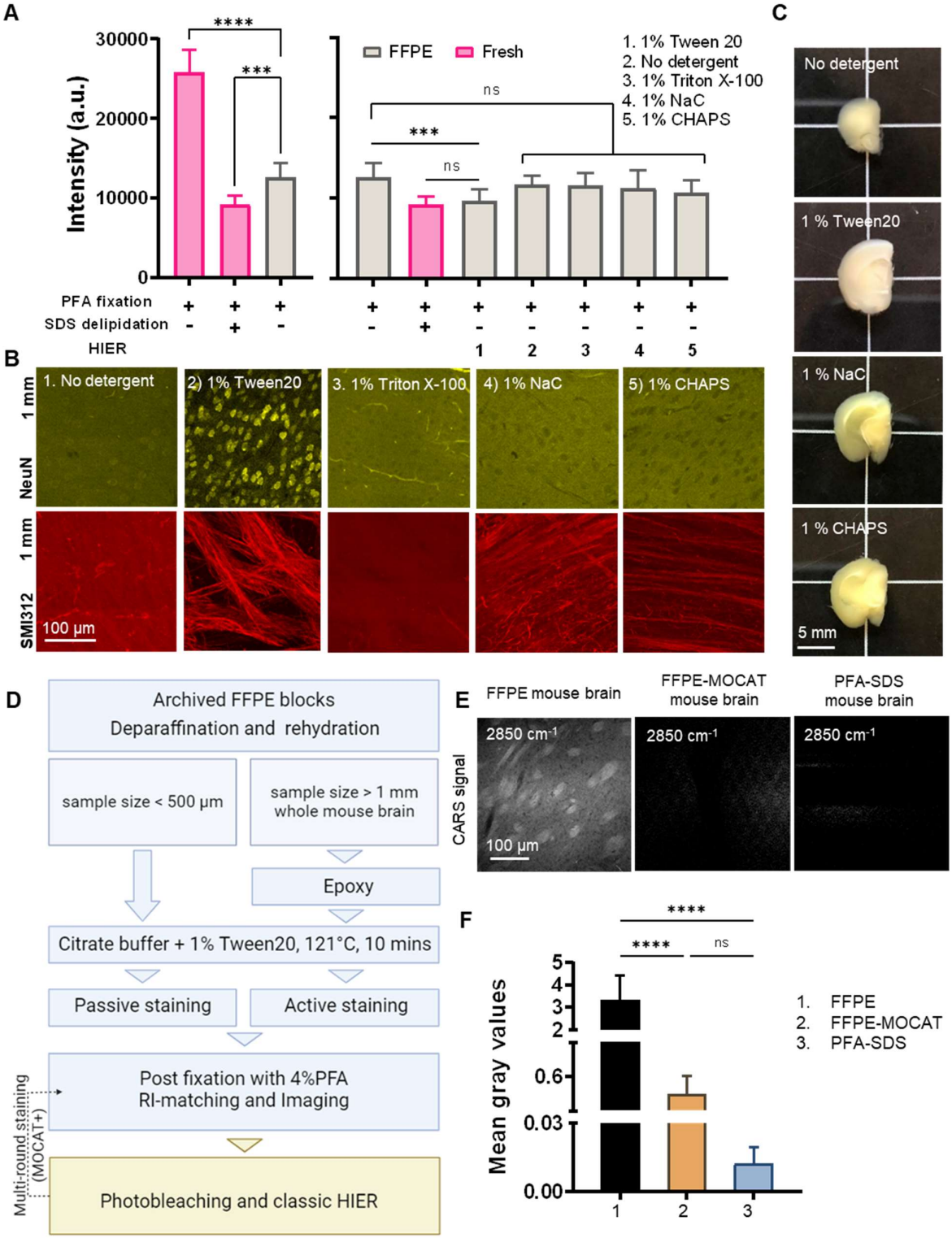
A
Intensity (a.u.)
30000
20000
10000
0
****
***
FFPE
Fresh
1. 1% Tween 20
2. No detergent
3. 1% Triton X-100
4. 1% NaC
5. 1% CHAPS
ns
***
ns
PFA fixation
SDS delipidation
HIER
1
2
3
4
5
B
1 mm
NeuN
1. No detergent
2) 1% Tween20
3. 1% Triton X-100
4) 1% NaC
5) 1% CHAPS
1 mm
SMI312
100 µm
C
No detergent
1 % Tween20
1 % NaC
1 % CHAPS
5 mm
D
Archived FFPE blocks
Deparaffination and rehydration
sample size < 500 µm
sample size > 1 mm
whole mouse brain
Epoxy
Citrate buffer + 1% Tween20, 121°C, 10 mins
Passive staining
Active staining
Post fixation with 4%PFA
RI-matching and Imaging
Multi-round staining
(MOCAT+)
Photobleaching and classic HIER
E
FFPE mouse brain
FFPE-MOCAT
mouse brain
PFA-SDS
mouse brain
CARS signal
2850 cm-1
2850 cm-1
2850 cm-1
100 µm
F
Mean gray values
5
4
3
2
0.6
0.03
0.00
****
****
ns
1
2
3
1. FFPE
2. FFPE-MOCAT
3. PFA-SDS

Figure 1. Development of the MOCAT pipeline.
(**A**) Comparison of DiD signal intensity in 2-mm-thick slices of undelipidated formaldehyde-fixed mouse brain, PFA-SDS mouse brain, and FFPE mouse brain treated under various detergent conditions.
(**B**) Multi-point confocal fluorescence images of neuronal nuclei in the cortex (top row) and axons in the striatum (bottom row) from 2-mm-thick FFPE mouse brain slices that had been treated under various detergent conditions. Images of optical sections captured at a depth of 1 mm are shown. Detergent types and concentrations are indicated. NeuN, a neuronal nuclear marker; SMI312, a pan-axonal marker.
(**C**) Gross views of 2-mm-thick slices of FFPE mouse brain treated under various detergent conditions.
(**D**) Schematic of the MOCAT pipeline.
(**E**) Images of coherent anti-Stokes Raman scattering (CARS) of dewaxed FFPE mouse brain, MOCAT-processed FFPE mouse brain, and PFA-SDS mouse brain. The images were taken at a Raman shift of 2850 cm^{-1} to address the CH2 vibration frequency.
(**F**) Statistical analysis of the gray values for the three treatment groups in (E). Gray values for 18 z-continuous images of each group were analyzed.
Statistical analysis: (A) n = 10; (E) n = 18. Mean ± SD, * $p < 0.05$, ** $p < 0.01$, *** $p < 0.001$, **** $p < 0.0001$, one-way ANOVA with Tukey's multiple comparison test.

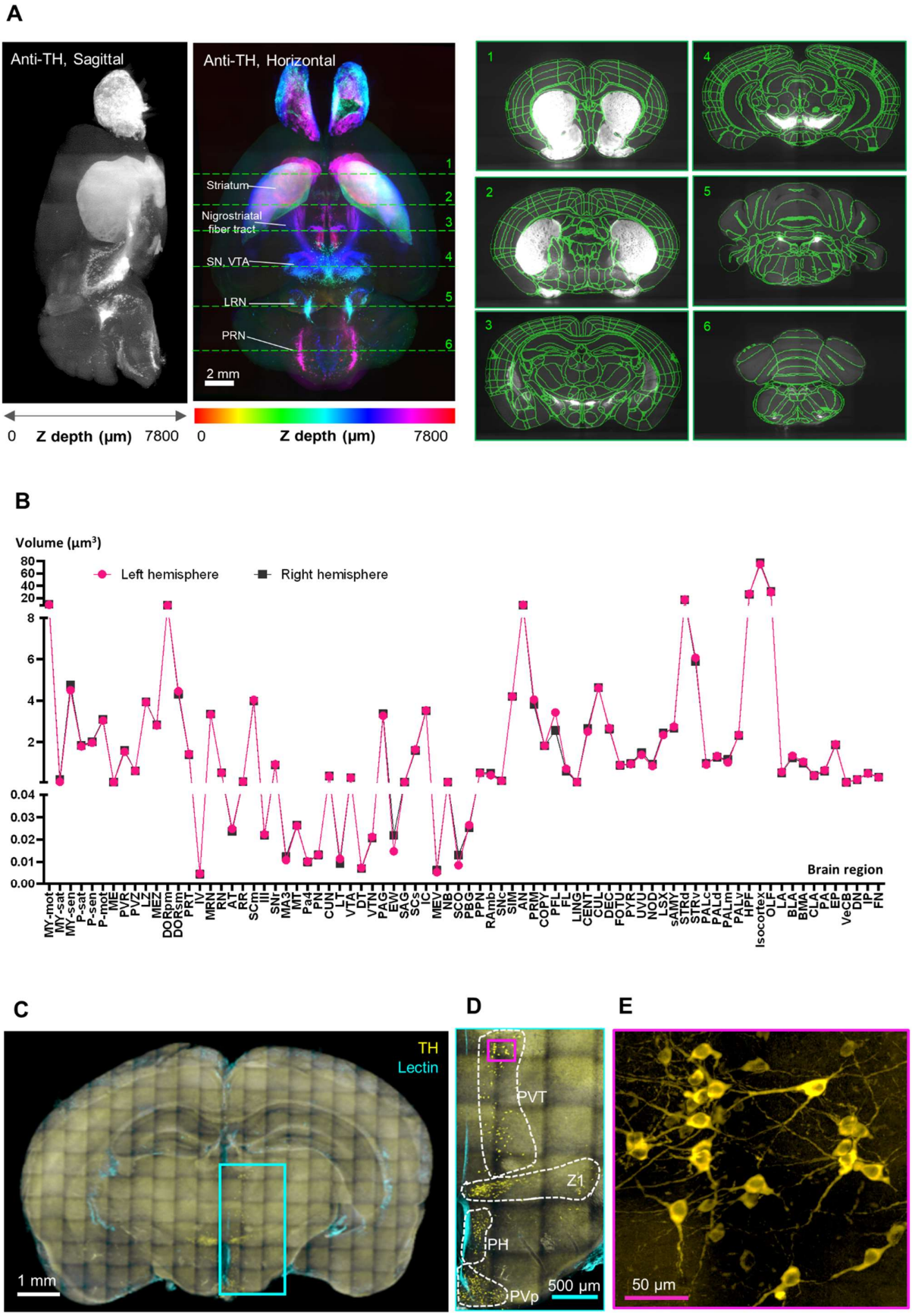
A
Anti-TH, Sagittal
Anti-TH, Horizontal
Striatum
Nigrostriatal fiber tract
SN, VTA
LRN
PRN
2 mm
0 Z depth (µm) 7800
0 Z depth (µm) 7800
B
Volume (µm³)
Left hemisphere
Right hemisphere
Brain region
MY-mot MY-sat MY-sen P-sat P-sen P-mot ME PVR PVZ LZ MEZ DORpm DORsm PRT IV MRN RN RT AR PR SCm III SNr MA3 MT Pa4 PN CUN LT VTA DT VTN PAG EW SAG SCs IC MEV NB SCO PBG PPN RAmb SNc SIM AN PRM COPY PFL FL LING CENT CUL DEC FOTU PYR UVU NOD LSX sAMY STRd STRv PALc PALd PALm PALv HPF Isocortex OLF LA BLA BMA CLA PA EP VeCB DN IP FN
C
TH
Lectin
1 mm
D
PVT
Z1
PH
PVp
500 µm
E
50 µm

Figure 2. Validation of the MOCAT pipeline.
(**A**) Brain-wide tyrosine hydroxylase (TH) expression (left panel) and registration (right panel) in FFPE-MOCAT C57BL/6 mouse brains. Whole mouse brain images were acquired using light-sheet microscopy, and the 3D-rendered images of the horizontal (XY) and sagittal (YZ) views are shown. Major dopaminergic regions are indicated: SN (substantia nigra), VTA (ventral tegmental area), LRN (lateral reticular nucleus), and PRN (pontine reticular nucleus). The results of brain registration for these regions (marked with green dotted lines and numbered in the XY view) are displayed from the coronal (XZ) view in the right panel.
(**B**) Comparison of brain region volumes between the left and right hemispheres of an FFPE-MOCAT mouse brain. All abbreviations are listed in Supplementary Table 2.
(**C** to **E**) Application of MOCAT to a 15-year-old FFPE block with TH-immunolabeling and multi-point confocal imaging. Specimen thickness: 2 mm.
(**C**) The projection image.
(**D**) Magnification of the cyan-lined region in (C). Dopaminergic regions are indicated. PVT, paraventricular nucleus of thalamus; PH, posterior hypothalamic nucleus; PVp, periventricular hypothalamic nucleus.
(**E**) Magnification of the magenta-lined region in (D). Scale bars are indicated in each panel.

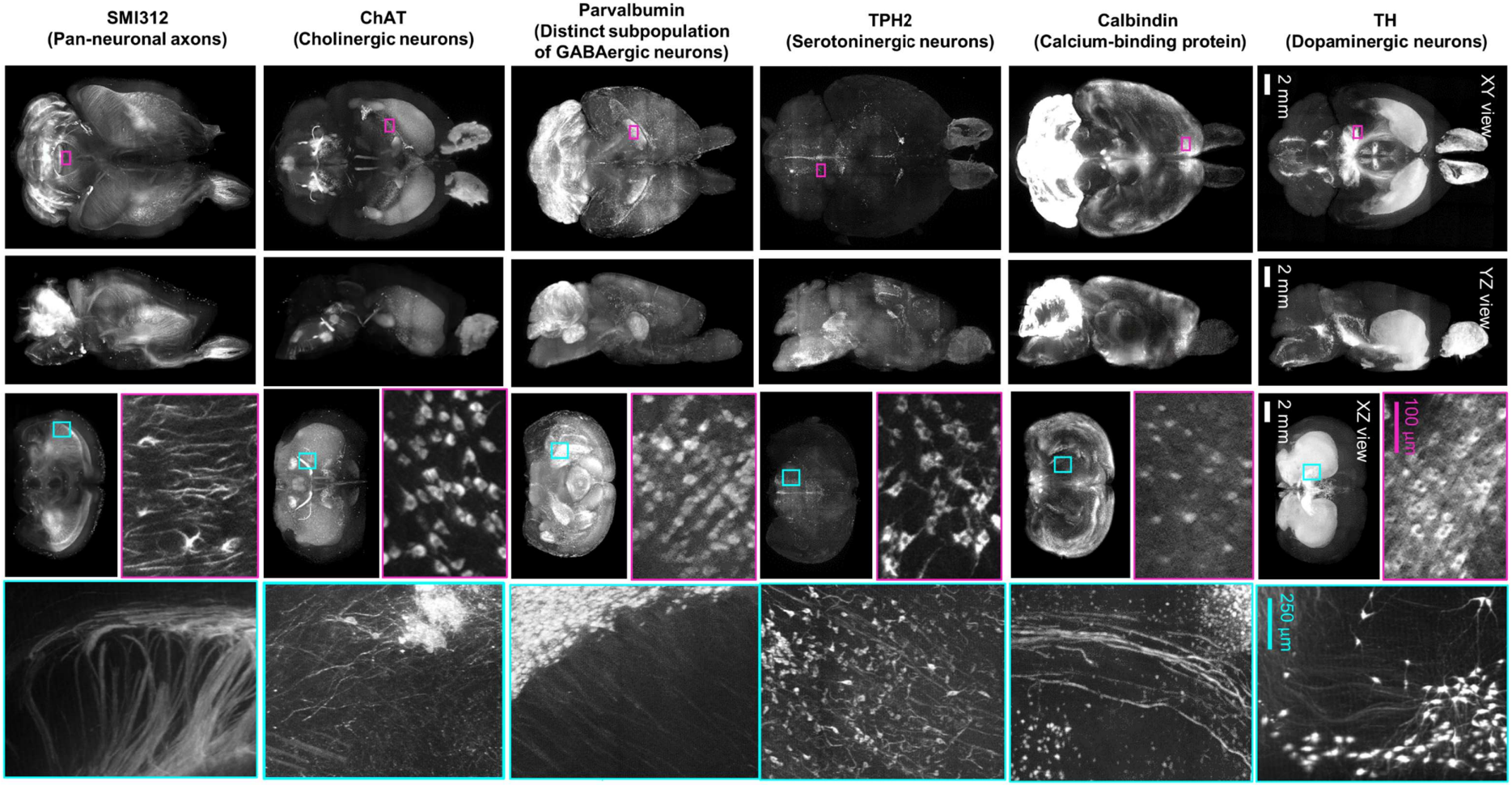
SMI312
(Pan-neuronal axons)
ChAT
(Cholinergic neurons)
Parvalbumin
(Distinct subpopulation
of GABAergic neurons)
TPH2
(Serotoninergic neurons)
Calbindin
(Calcium-binding protein)
TH
(Dopaminergic neurons)
XY view
YZ view
XZ view
2 mm
100 µm
250 µm

Figure 3. Multi-round immunostaining of FFPE-MOCAT whole mouse brain (MOCAT+). Light-sheet microscopy imaging datasets of six-round immunolabeling performed on one whole FFPE mouse brain. Projection images of the horizontal (XY), sagittal (YZ), and transverse (XZ) views are shown. Projection images (200-µm thick) of magenta-lined and cyan-lined regions marked in the XY and XZ views are magnified and displayed within correspondingly colored frames. Scale bars are indicated in the first row.

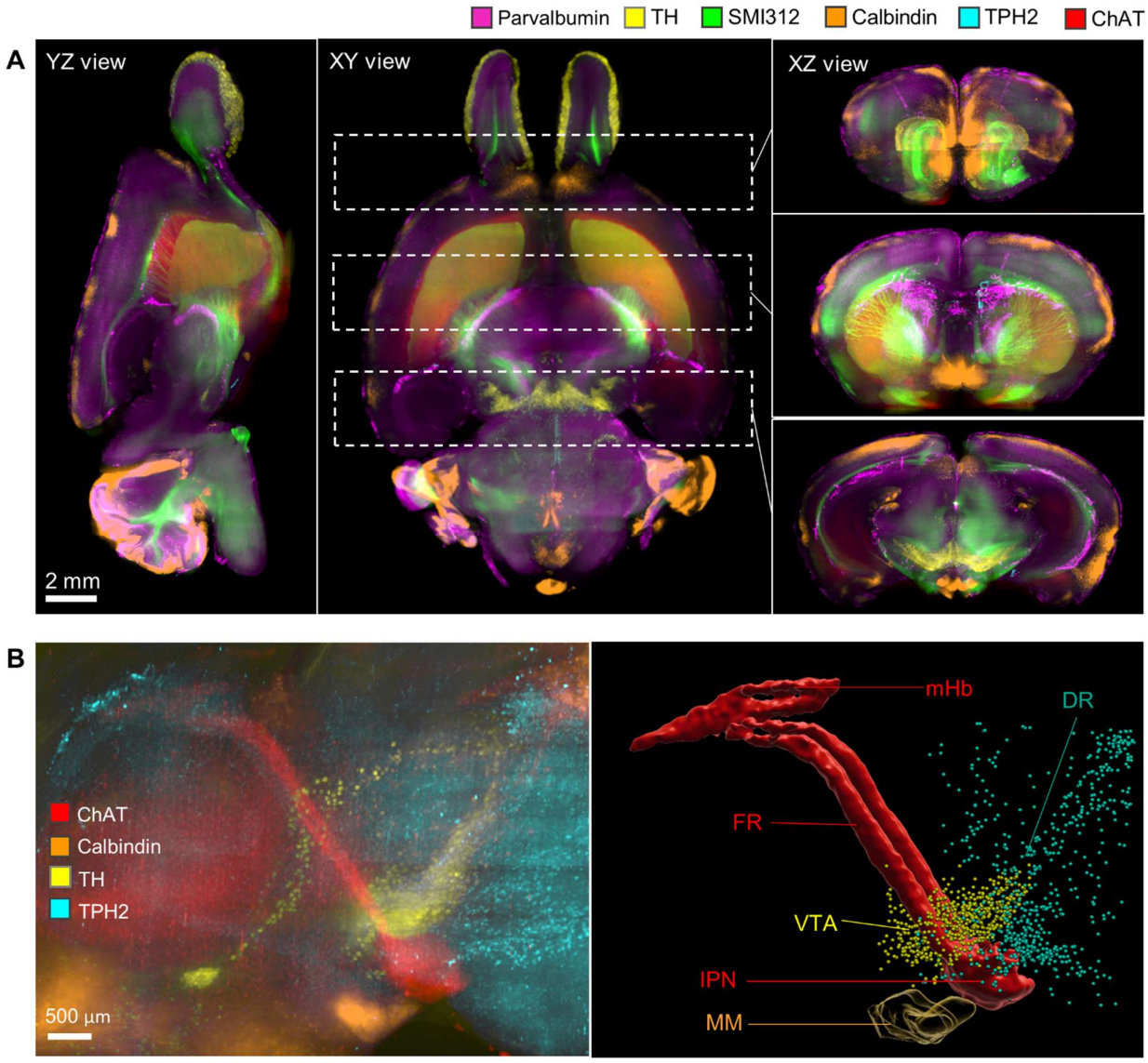

Figure 4. Merged multichannel neuron circuitry image generated by MOCAT+.
(**A**) Merged multichannel image generated using the datasets from Fig. 3. Optical sections from the horizontal (XY) and sagittal (YZ) perspectives are presented. For the transverse (XZ) views, projection images of the regions encompassed by the dotted lines in the XY view are displayed. (**B**) The spatial relationship of the Hbn-IPN circuitry, dopaminergic (TH), serotoninergic (TPH2), and calbindin+ GABAergic neurons. Fluorescence (right) and segmented (left) images are shown. mHb, medial habenula; FR, fasciculus retroflexus; IPN, interpeduncular nucleus; SuM, medial mammillary area of the hypothalamus; DR, dorsal raphe nuclei.

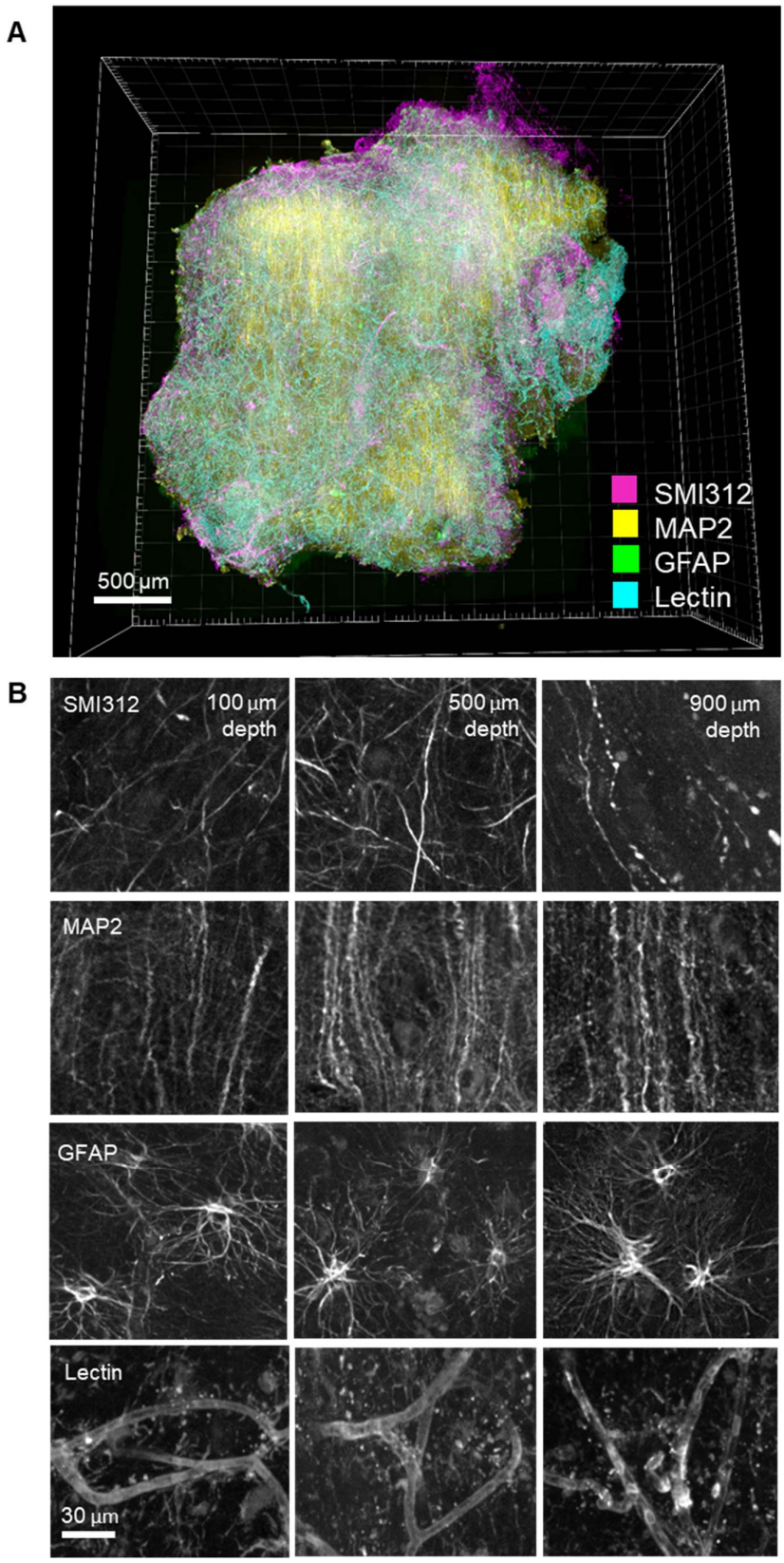
A
SMI312
MAP2
GFAP
Lectin
500 µm
B
SMI312
100 µm depth
500 µm depth
900 µm depth
MAP2
GFAP
Lectin
30 µm

Figure 5. Multi-round immunostaining of a FFPE-MOCAT human brain specimen.
Three-round immunolabeling was performed on a FFPE human brain specimen collected from a patient with cerebral hemorrhage. Images were acquired using multi-point confocal microscopy.
(**A**) 3D rendering of the entire specimen.
(**B**) Images depicting merged and single channels of an optical section from the selected area (white frame) in (A) at depths of 100 μm, 500 μm, and 900 μm. GFAP: Glial fibrillary acidic protein; SMI312: pan-axonal marker; MAP2: microtubule-associated protein 2 (a dendritic marker).

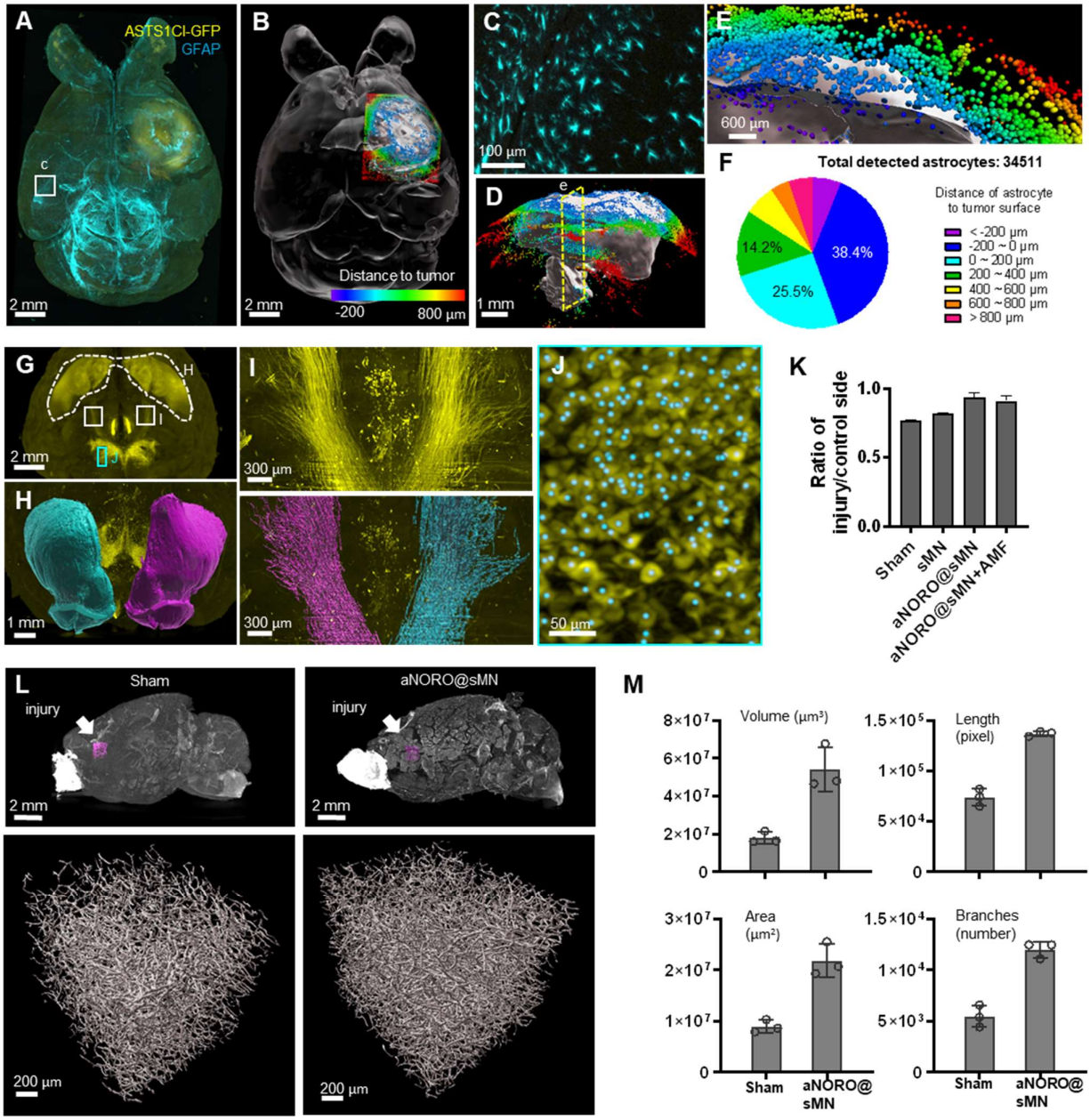
A
ASTS1CI-GFP
GFAP
c
2 mm
B
Distance to tumor
-200
800 μm
2 mm
C
100 μm
D
e
1 mm
E
600 μm
F
Total detected astrocytes: 34511
Distance of astrocyte to tumor surface
< -200 μm
-200 ~ 0 μm
0 ~ 200 μm
200 ~ 400 μm
400 ~ 600 μm
600 ~ 800 μm
> 800 μm
38.4%
25.5%
14.2%
G
H
I
J
2 mm
1 mm
300 μm
50 μm
K
Ratio of injury/control side
1.0
0.5
0.0
Sham
sMN
aNORO@sMN
aNORO@sMN+AMF
L
Sham
aNORO@sMN
injury
2 mm
200 μm
M
Volume (μm³)
Length (pixel)
Area (μm²)
Branches (number)
Sham
aNORO@sMN

Figure 6. Applications of MOCAT in disease models.
(**A** to **F**) MOCAT reveals cell-tumor relationships in an astrocytoma model.
(**A**) Projection light-sheet image of a FFPE-MOCAT mouse brain with a GFP-expressing astrocytoma xenograft (ALTS1C1 cells, see Materials and Methods) stained for GFP (yellow) and GFAP (cyan).
(**B**) Segmented tumor (white) and surrounding astrocytes (colored). The astrocytes are colored according to the color-coded scale of cell-to-tumor distance.
(**C**) Magnification of the region marked in (A), showing astrocyte morphology.
(**D**) Sagittal view of the segmented tumor and color-coded astrocytes.
(**E**) Magnification of the clipping plane marked in (D, yellow dashed line), showing astrocytes inside (dark blue, purple) and outside (red, orange, yellow, green, cyan, blue) the tumor.
(**F**) Quantification of detected astrocytes and their classification according to distance to the tumor surface.
(G to M) MOCAT reveals brain damage and the therapeutic effect of alternating magnetic field-responsive NO-release octahedrons (aNORO) administered using a paracetamol-coated silk-based microneedle (sMN) in a TBI mouse model.
(G to J) Segmentation of dopaminergic regions in FFPE-MOCAT TBI mouse brains.
(G) Whole-brain projection light-sheet image focusing on TH-positive regions.
(**H**) Frontal view of the segmented striatum (dashed white line in (G)). Magenta: the injured side; cyan: the contralateral side.
(**I**) Horizontal views of the nigrostriatal fiber tract (paired white boxes in (G)); fluorescence (top) and segmented (bottom) images are shown. Magenta: the injured side; cyan: the contralateral side.
(J) Detection of dopaminergic cells in the substantia nigra (SN). Magnification of the marked area in (G), including the TH fluorescence signal (yellow) and segmented cells (cyan dots).
(**K**) Comparison of the therapeutic effects of different treatments. $n = 3$ (three indicators: striatum volume, nigrostriatal fiber tract volume, SN cell number), mean ± SD, * $p < 0.05$, ** $p < 0.01$, *** $p < 0.001$, **** $p < 0.0001$, one-way ANOVA with Tukey's multiple comparison test.
(**L**) Reconstruction of blood vessels in TBI brains with or without treatments. The regions of interest (ROIs) selected to assess angiogenesis are indicated in the top row (magenta boxes, directly below the injury site). 3D reconstructions of blood vessels are shown in the bottom row.
(M) Quantification of blood vessel volume, blood vessel surface area, number of blood vessel branches, and blood vessel length. $n = 3$, mean ± SD have been plotted.

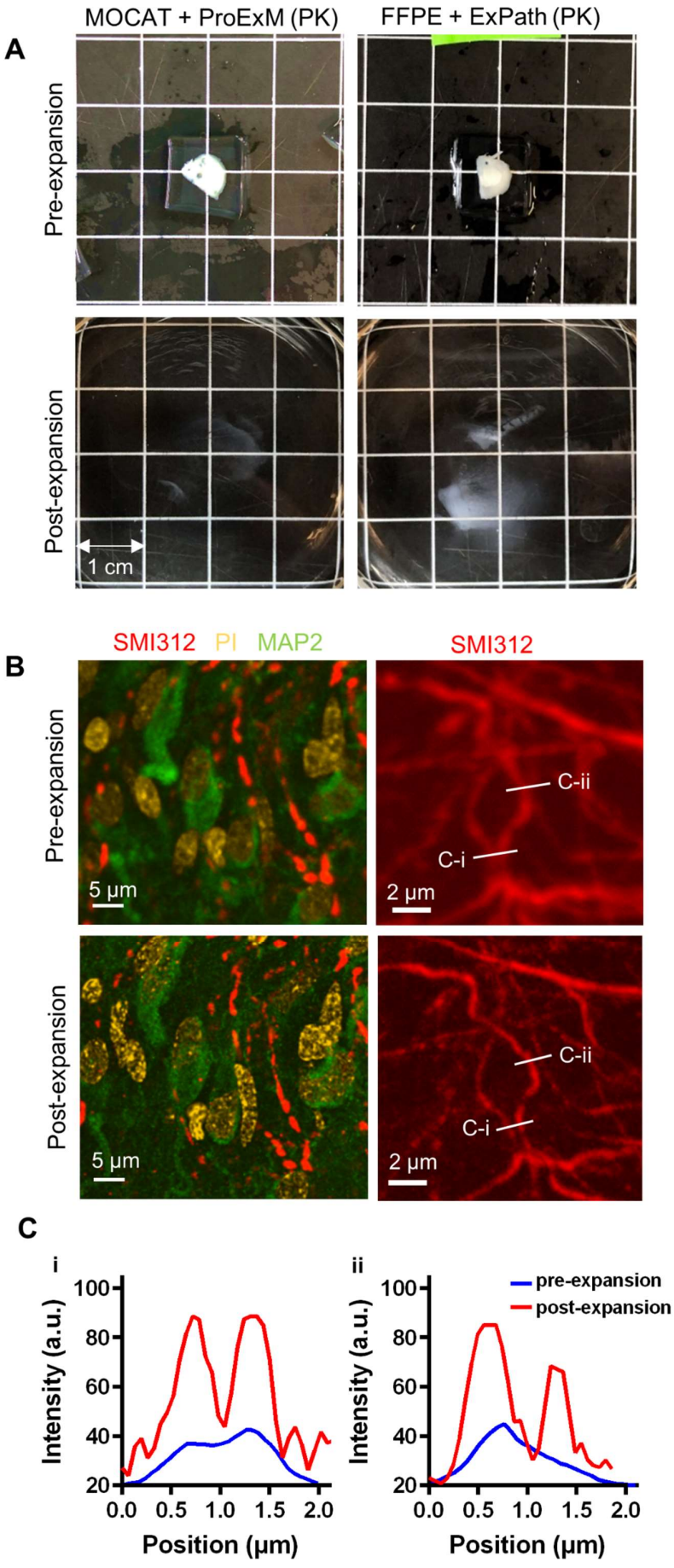
A
MOCAT + ProExM (PK)
FFPE + ExPath (PK)
Pre-expansion
Post-expansion
1 cm
B
SMI312 PI MAP2
SMI312
Pre-expansion
Post-expansion
C-ii
C-i
5 µm
2 µm
C
i
ii
Intensity (a.u.)
Position (µm)
pre-expansion
post-expansion
0.0 0.5 1.0 1.5 2.0
20 40 60 80 100

Figure 7. Expansion microscopy on a FFPE-MOCAT human brain specimen.
(**A**) Gross views of expansion of a 1-mm FFPE specimen.
(**B**) Fluorescence images of a FFPE human brain pre- (top row) and post-expansion (bottom row). Left: merged images of multiplexed staining; right: fluorescence images of SMI312 staining.
(**C**) Profiles of axon signal intensity taken along the white lines shown in the images of the right panel in (B). The scale bar has been divided by the expansion factor.